

# Insights into the mechanisms of optical cavity-modified ground-state chemical reactions

Yaling Ke<sup>1</sup> and Jeremy Richardson<sup>1</sup>

*Department of Chemistry and Applied Biosciences, ETH Zürich, 8093 Zürich, Switzerland*

(\*Electronic mail: yaling.ke@phys.chem.ethz.ch)

(Dated: 23 December 2023)

In this work, we systematically investigate the mechanisms underlying the photon frequency-dependent rate modification of ground-state chemical reactions in an optical cavity, as well as the effects of the collective coupling of two molecules to the same cavity photon mode. Our analysis is grounded in a symmetric double-well description of the molecular potential energy surface. To obtain reaction dynamics, we employ a numerically exact open quantum system approach, namely, the hierarchical equations of motion in twin space with a matrix product state solver. Our results reveal that the reaction rate can be modified when the cavity frequency closely matches the transition energy between a pair of vibrational eigenstates. This modification arises due to the opening of a cavity-induced intra-molecular cotunneling pathway, and the extent of rate modification is determined jointly by several kinetic factors. For an anharmonic molecular system with multiple vibrational transition energies, we predict the possibility of observing multiple peaks in the photon frequency-dependent rate profile. Increasing the light-matter coupling strength not only enhances the intensity and the width of the peaks in the rate profile but may also lead to the fusion of two nearby peaks. Furthermore, we find that when two identical molecules are simultaneously coupled to the same resonant cavity mode, an intermolecular reaction channel is activated, contributing to a further alternation in the reaction rate. It is worth emphasizing that, the rate modification due to these intramolecular and intermolecular cavity-promoted reaction pathways remains unaffected regardless of whether the molecular transition dipoles are aligned in the same or opposite direction as the light polarization. This suggests that the cavity-induced rate modification can persist in an isotropically disordered system, differing inherently from the influence of direct intermolecular dipolar interaction, which shows an opposite rate modification tendency in these two dipole orientations.

## I. INTRODUCTION

In recent years, a series of experiments has reported that the kinetics of ground-state chemical reactions can be altered within a photonic structure,<sup>1–11</sup> such as a microfluidic Fabry-Pérot cavity.<sup>12</sup> In this configuration, the frequency of optical modes can be adjusted by varying the distance between two parallel dielectric mirrors, which are separated by a few micrometers. Notably, the reaction rate undergoes the most significant modification when the cavity photon frequency is finely tuned to match the molecular vibrational absorption bands. This discovery has evolved into a burgeoning field known as polariton chemistry. On the one hand, it provides a gateway to constructing a more fundamental and profound understanding of chemical reaction mechanisms. On the other hand, it presents a promising strategy for controlling molecular chemical reactivity in a non-intrusive and selective manner.<sup>13,14</sup>

Despite a great number of theoretical studies on this topic,<sup>15–33</sup> a clear and comprehensive understanding of the underlying physicochemical processes that enhance or suppress chemical reactivities remains largely elusive.<sup>34</sup> To study chemical reactions in an optical cavity, a full account of complex interactions among molecules, their numerous solvent degrees of freedom (DoF), as well as the electromagnetic radiation modes inside and outside the cavity, proves to be necessary.<sup>35,36</sup> Recently, a few fully quantum-mechanical studies utilizing the numerically exact hierarchical equation of motion (HEOM) approach have successfully produced a correct resonance structure of the cavity frequency-dependent

rate profile.<sup>37,38</sup> This means that rate modification peaks in proximity to the molecular vibrational frequency. However, to the best of our knowledge, an explicit explanation regarding the origin of this resonance structure is still lacking. Furthermore, these studies are conducted in the single-molecule limit, which differs from the experimental conditions where a large number of molecules are collectively coupled to the cavity modes.

In this work, our first objective is to gain a deeper insight into the reaction mechanisms underlying the modification of chemical reactivity induced by an optical cavity. Secondly, we aim to go beyond the single-molecule limit by considering two molecules inside the cavity, examining the impact of the collective effect and intermolecular coupling on the reaction rate. To address this challenging problem, we utilize the recently developed HEOM method in twin space.<sup>39–41</sup> This method maps the HEOM for a set of auxiliary density matrices into a time-dependent Schrödinger equation for an extended pure state wave function. Through the application of matrix product state (MPS) decomposition<sup>42</sup> (also known as tensor train<sup>43</sup> (TT)) of the extended wave function, and a tangent-space time propagation scheme,<sup>44–46</sup> we significantly extend the applicability of the HEOM method to a much larger system.

The remainder of this work is organized as follows: in Sec. II, we first delineate an open quantum system model describing a molecular aggregate embedded in solvent and an optical cavity environment. Following that, we provide a brief introduction to the HEOM+MPS/TT method and the observables of interest. Subsequently, in Sec. III, we present the simulation details and discuss results for a series of models with increasing complexity: a single molecule inside and outside

the cavity, as well as two molecules inside the cavity. Finally, a summary of the underlying reaction mechanisms and prospects for future works are provided in Sec. IV.

## II. THEORY

### A. Model

To investigate ground-state molecular reaction dynamics within an optical cavity, as schematically illustrated in Fig. 1(a), we employ the Pauli-Fierz light-matter Hamiltonian in the dipole gauge and under the long-wavelength approximation.<sup>34,37,47,48</sup>

$$H = H_{\text{mol}} + H_{\text{sol}} + H_{\text{cav}} + H_{\text{cbath}}, \quad (1)$$

where  $H_{\text{mol}}$  is the molecular Hamiltonian,  $H_{\text{sol}}$  considers the solvent DoFs,  $H_{\text{cav}}$  corresponds to the radiation modes inside the cavity, and  $H_{\text{cbath}}$  describes a photon bath outside the cavity. For convenience, we set  $\hbar = 1$  throughout this work.

For the molecular system, we consider an aggregate with  $N_{\text{mol}}$  molecules, where each molecule is represented by a single reactive vibrational DoF, and the Hamiltonian is given by

$$H_{\text{mol}} = \sum_{i=1}^{N_{\text{mol}}} \left[ \frac{p_i^2}{2M_i} + V(x_i) \right] + \sum_{i' < i} \Delta_{ii'} \vec{\mu}_i(x_i) \cdot \vec{\mu}_{i'}(x_{i'}). \quad (2)$$

Here  $p_i$ ,  $x_i$ , and  $M_i$  are the momentum, coordinate, and effective mass of the reaction coordinate of the  $i$ th molecule, respectively. We assume that the ground-state potential  $V(x)$  along the reaction coordinate  $x$  takes a symmetric double-well form,

$$V(x) = \frac{\omega_b^4}{16E_b} x^4 - \frac{1}{2} \omega_b^2 x^2, \quad (3)$$

where  $E_b$  is the barrier height between two local minima and  $\omega_b$  is the barrier frequency. The second term on the r.h.s. of Eq. (2) describes the dipole-dipole interaction between the  $i$ th and  $i'$ th molecule with the strength  $\Delta_{ii'}$ . The vectorial molecular dipole moments  $\vec{\mu}_i(x_i)$  are projected onto the electronic ground state.

Every molecule is surrounded by a multitude of solvent molecules. Therefore, we assume that every molecule is coupled to its own environment, which is modeled as a bosonic bath comprising infinite harmonic oscillators,

$$H_{\text{sol}} = \sum_{i=1}^{N_{\text{mol}}} \sum_k \left[ \frac{P_{ik}^2}{2} + \frac{1}{2} \omega_{ik}^2 \left( Q_{ik} + \frac{c_{ik} x_i}{\omega_{ik}} \right)^2 \right]. \quad (4)$$

Here,  $P_{ik}$  and  $Q_{ik}$  are the conjugate momentum and coordinate of the  $k$ th oscillator with the frequency  $\omega_{ik}$ , in the neighborhood of the  $i$ th molecule. Every oscillator in the molecular bath is displaced by  $c_{ik} x_i / \omega_{ik}^2$  due to its coupling to the molecule, and  $c_{ik}$  denotes the coupling strength.

The cavity Hamiltonian is expressed as

$$H_{\text{cav}} = \frac{p_c^2}{2} + \frac{1}{2} \omega_c^2 \left( x_c + \sqrt{\frac{2}{\omega_c}} \eta_c \sum_{i=1}^{N_{\text{mol}}} \vec{\mu}_i(x_i) \cdot \vec{e} \right)^2, \quad (5)$$

which contains a quantized radiation mode and the light-matter interaction. The cavity photon mode is characterized as a harmonic oscillator with the momentum  $p_c$ , coordinate  $q_c$ , and the frequency  $\omega_c$ . The light-matter coupling strength is given by the unitless parameter  $\eta_c = \frac{1}{\omega_c} \sqrt{\frac{\omega_c}{2\epsilon_0 V}}$  where  $\epsilon_0$  is the permittivity of the medium in the cavity and  $V$  is the quantization volume of the electromagnetic mode. The unit vector  $\vec{e}$  points to the light polarization direction.

In practice, the cavity mirrors are not perfectly reflective. The cavity photon mode can interact with the continuum of far-field electromagnetic modes outside of the cavity, leading to the influx or efflux of photons in the cavity. This interaction is described by the Hamiltonian

$$H_{\text{cbath}} = \sum_j \frac{P_j^2}{2} + \frac{1}{2} \omega_j^2 \left( Q_j + \frac{c_j}{\omega_j^2} x_c \right)^2, \quad (6)$$

where  $P_j$ ,  $Q_j$ , and  $\omega_j$  are the momentum, coordinate, and frequency of the photon modes outside the cavity, and the coupling strength is specified by  $c_j$ . We should mention that Eq. (6) is usually termed as cavity loss, which would be more appropriate in the case where the cavity photon bath is Markovian and there is no reflux of the photon back into the cavity.

The model in Eq. (1) can be considered as an open quantum system, that is, a system of interest interacting with a macroscopic environment,

$$H = H_{\text{sys}} + H_{\text{env}} + H_{\text{int}}, \quad (7)$$

as schematically illustrated in Fig. 1(b). The molecules and the cavity photon mode constitute the system of interest and the system Hamiltonian is defined as

$$H_{\text{sys}} = H_{\text{mol}} + H_{\text{cav}} + H_{\text{ren}}, \quad (8)$$

where the reorganization term is  $H_{\text{ren}} = \sum_i \lambda_i x_i^2 + \lambda_c x_c^2$  with  $\lambda_i = \sum_k \frac{c_{ik}^2}{2\omega_{ik}^2}$  and  $\lambda_c = \sum_j \frac{c_j^2}{2\omega_j^2}$ . The environment includes all unshifted harmonic oscillators in the solvents (see Eq. (4)) and cavity photon bath (see Eq. (6)),

$$H_{\text{env}} = \sum_{i=1}^{N_{\text{mol}}} \sum_k \left[ \frac{P_{ik}^2}{2} + \frac{1}{2} \omega_{ik}^2 Q_{ik}^2 \right] + \sum_j \left[ \frac{P_j^2}{2} + \frac{1}{2} \omega_j^2 Q_j^2 \right]. \quad (9)$$

The system-environment interaction is then given by

$$H_{\text{int}} = \sum_{i=1}^{N_{\text{mol}}} \sum_k c_{ik} x_i Q_{ik} + \sum_j c_j x_c Q_j. \quad (10)$$

The form of the Hamiltonian is such that we can exploit the open quantum system approach, specifically the hierarchical equation of motion,<sup>49–53</sup> to obtain the system dynamics.

### B. Open quantum system approach - HEOM+MPS/TT method

At the initial moment, we assume that the system and the environment are factorized and the environment is in

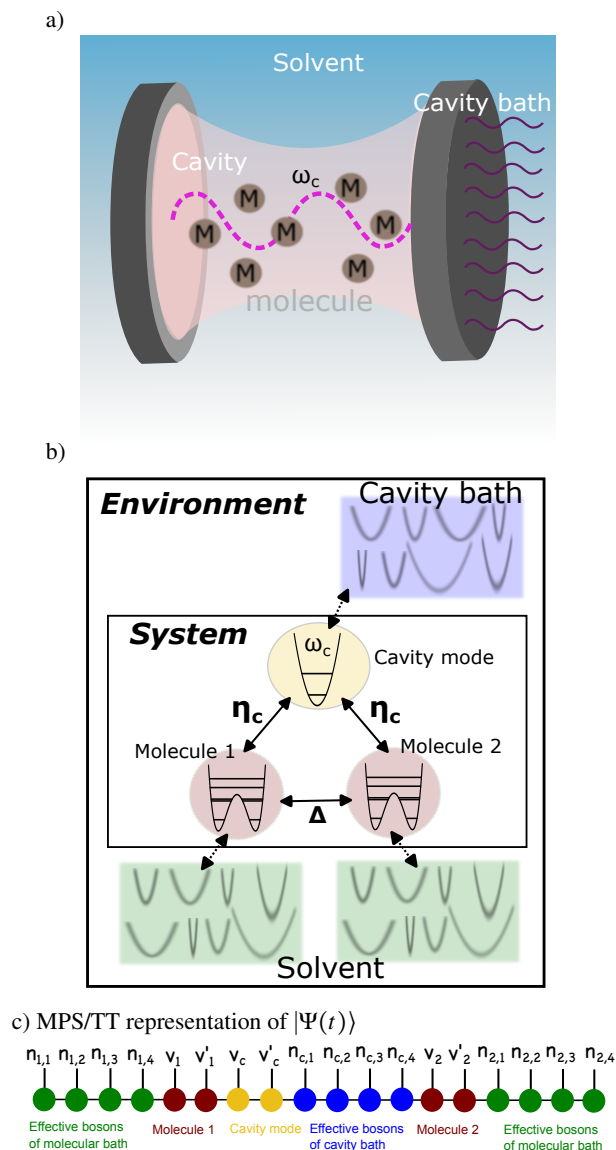


FIG. 1. a) Sketch of molecules in an optical cavity. The molecules are immersed in a solvent, and the radiation mode inside the cavity is coupled to far-field electromagnetic modes outside the cavity. b) Schematic illustration of an open quantum system model for the Pauli-Fierz light-matter Hamiltonian in Eq. (1). As an example, we showcase two molecules and one cavity mode in the system. Each molecule is coupled to its respective bosonic phonon bath, while the cavity mode interacts with its bosonic photon bath. c) Optimal arrangement of all physical degrees of freedom as a one-dimensional tensor train for the extended wavefunction  $|\Psi(t)\rangle$ , corresponding to the open quantum system model depicted above.

its own thermal equilibrium at an inverse temperature  $\beta = 1/(k_B T)$  with the Boltzmann constant  $k_B$  and the temperature  $T$ . The initial density operator for the composite system-plus-

environment is given by

$$\rho(0) = \rho_{\text{sys}}(0) \cdot \frac{e^{-\beta H_{\text{env}}}}{\text{Tr}_{\text{env}} \{e^{-\beta H_{\text{env}}}\}}, \quad (11)$$

where  $\text{Tr}_{\text{env}}$  denotes tracing over the environmental DoFs. In the reduced description of the system dynamics,

$$\rho_{\text{sys}}(t) = \text{Tr}_{\text{env}} \{\rho(t)\}, \quad (12)$$

the environmental influence is fully encoded in the time-correlation function

$$C_\alpha(t) = \frac{1}{\pi} \int_{-\infty}^{\infty} \frac{e^{-i\omega t}}{1 - e^{-\beta\omega}} J_\alpha(\omega) d\omega, \quad (13)$$

where  $J_\alpha(\omega)$  is the coupling-weighted density of states in the frequency space of bath  $\alpha$  in the environment. The spectral density function for the bath coupled to the  $i$ th molecule is given by

$$J_i(\omega) = \frac{\pi}{2} \sum_k \frac{c_{ik}^2}{\omega_{ik}} \delta(\omega - \omega_{ik}), \quad (14)$$

and that for the cavity photon bath is

$$J_c(\omega) = \frac{\pi}{2} \sum_j \frac{c_j^2}{\omega_j} \delta(\omega - \omega_j). \quad (15)$$

In this work, we use the Debye-Lorentzian spectral density function

$$J_\alpha(\omega) = \frac{2\lambda_\alpha \omega \Omega_\alpha}{\omega^2 + \Omega_\alpha^2}. \quad (16)$$

with two parameters, the reorganization energy  $\lambda_\alpha$  and the characteristic frequency  $\Omega_\alpha$  for bath  $\alpha$ .

The time correlation function in Eq. (13) can be expressed as a sum over exponentials<sup>54,55</sup>

$$C_\alpha(t) = \sum_{p=0} \lambda_\alpha \eta_{\alpha p} e^{-i\gamma_{\alpha p} t}. \quad (17)$$

This exponential expansion is a crucial step in deriving the HEOM method. In practical implementation, the summation can be truncated at a finite number of terms, denoted as  $P$ . For a detailed description of the method, we refer readers to Ref. 53 and the literature therein. Here, we only briefly introduce the main ideas of the method in twin space.<sup>39-41</sup>

Every component in Eq. (17) can be interpreted as a dissipative bosonic mode with a complex-valued frequency  $\gamma_{\alpha p}$  and coupling strength to the system  $\eta_{\alpha p}$ . A specific configuration  $\mathbf{n}_\alpha = (n_{\alpha 0}, n_{\alpha 1}, n_{\alpha 2}, \dots, n_{\alpha P})$  specifies the state with  $n_{\alpha p}$  phonons in the  $p$ th bosonic mode ( $p$  runs from 0 to  $P$ ) of bath  $\alpha$ . For a super index  $\mathbf{n} = (\dots, \mathbf{n}_\alpha, \dots)$ , one can introduce an auxiliary density operator (ADO)  $\rho^{\mathbf{n}}(t)$ . This set of auxiliary density operators is closed with respect to the time-derivative operation and yields a hierarchical equation of motion

$$i \frac{d\rho^n(t)}{dt} = [H_{\text{sys}}, \rho^n(t)] - i \sum_{\alpha} \sum_p n_{\alpha p} \gamma_{\alpha,p} \rho^n(t) + \sum_{\alpha} \sum_p \sqrt{\lambda_{\alpha}(n_{\alpha p} + 1)} (x_{\alpha} \rho^{n_{\alpha p}^+}(t) - \rho^{n_{\alpha p}^+}(t) x_{\alpha}) + \sum_{\alpha} \sum_p \sqrt{\lambda_{\alpha} n_{\alpha p}} (\eta_{\alpha p} x_{\alpha} \rho^{n_{\alpha p}^-}(t) - \eta_{\alpha p}^* \rho^{n_{\alpha p}^-}(t) x_{\alpha}). \quad (18)$$

Here,  $\mathbf{n}_{\alpha p}^{\pm} = (\dots, n_{\alpha p} \pm 1, \dots)$ . When all dissipative modes are in their ground state, i.e.  $\mathbf{n} = (0 \dots 0)$ , the ADO  $\rho^{\mathbf{n}=0}(t)$  is exactly the reduced density operator  $\rho_{\text{sys}}(t)$ .

Each ADO can be expressed in twin space as a rank- $2N_{\text{sys}}$  tensor,

$$|\rho^n(t)\rangle\rangle \equiv \sum_{v_1, v'_1, \dots, v_{N_{\text{sys}}}, v'_{N_{\text{sys}}}} C_{v_1 v'_1, \dots, v_{N_{\text{sys}}} v'_{N_{\text{sys}}}}^{\mathbf{n}}(t) |v_1 v'_1 \dots v_{N_{\text{sys}}} v'_{N_{\text{sys}}}\rangle. \quad (19)$$

For the model system in Sec. II A, we have  $N_{\text{sys}} = N_{\text{mol}} + 1$ . In Eq. (19), the  $\alpha$ th physical DoF in the system is represented by two independent indices,  $v_{\alpha}$  and  $v'_{\alpha}$ . Accordingly, a single operator  $O_{\alpha}$  for the  $\alpha$ th DoF is related to a pair of superoperators in twin space,  $\hat{O}_{\alpha} = O_{\alpha} \otimes I_{\alpha}$  and  $\tilde{O}_{\alpha} = I_{\alpha} \otimes O_{\alpha}^{\dagger}$ , where  $I_{\alpha}$  is a unit operator. The whole set of ADOs forms an extended wave function

$$|\Psi(t)\rangle = \sum_{n_0 \dots n_{\alpha p} \dots n_{N_{\text{sys}} p}} |\rho^n(t)\rangle\rangle \otimes |\mathbf{n}\rangle. \quad (20)$$

Further, we introduce a pair of creation and annihilation operators,  $b_{\alpha p}^+$  and  $b_{\alpha p}$ , which act on  $|\mathbf{n}\rangle$  to yield

$$b_{\alpha p}^+ |\mathbf{n}\rangle = \sqrt{n_{\alpha p} + 1} |\mathbf{n}_{\alpha p}^+\rangle; \quad (21a)$$

$$b_{\alpha p} |\mathbf{n}\rangle = \sqrt{n_{\alpha p}} |\mathbf{n}_{\alpha p}^-\rangle. \quad (21b)$$

Then, Eq. (18) can be recast into a Schrödinger equation for the wave function  $|\Psi(t)\rangle$ ,

$$i \frac{d|\Psi(t)\rangle}{dt} = \mathcal{H} |\Psi(t)\rangle, \quad (22)$$

with the super-Hamiltonian

$$\mathcal{H} = \hat{H}_{\text{sys}} - \tilde{H}_{\text{sys}} - i \sum_{\alpha} \sum_p \gamma_{\alpha p} b_{\alpha p}^+ b_{\alpha p} + \sum_{\alpha} \sum_p \sqrt{\lambda_{\alpha}} [(\hat{x}_{\alpha} - \tilde{x}_{\alpha}) b_{\alpha p} + (\eta_{\alpha p} \hat{x}_{\alpha} - \eta_{\alpha p}^* \tilde{x}_{\alpha}) b_{\alpha p}^+]. \quad (23)$$

The high-rank coefficient tensor  $C_{s_1 s'_1, \dots, s_{N_{\text{sys}}} s'_{N_{\text{sys}}}}^{\mathbf{n}}(t)$  in the extended wave function can be decomposed in the matrix product state formalism as

$$C_{s_1 s'_1, \dots, s_{N_{\text{sys}}} s'_{N_{\text{sys}}}}^{\mathbf{n}}(t) = \sum_{r_0, r_1, \dots, r_{2N_{\text{sys}}+K}} A_{r_0, r_1, v_1}^{[1]}(t) A_{r_1, r_2, v'_1}^{[2]}(t) \dots A_{r_{2N_{\text{sys}}+K-1}, r_{2N_{\text{sys}}+K}, n_K}^{[2N_{\text{sys}}+K]}(t), \quad (24)$$

where  $K = N_{\text{sys}}(P + 1)$ . An example of the MPS/TT decomposition of  $|\Psi(t)\rangle$  is shown schematically in Fig. 1(c). Here,  $\{A^{[k]}\}$  are rank-3 tensors, with one index being either  $v_i$ ,  $v'_i$ , or  $n_{\alpha p}$ , and the other two virtual indices  $r_{k-1}$  and  $r_k$  corresponding the bond connecting the neighboring tensors. The virtual index  $r_k$  runs from 1 to  $D_k$ , where the bond dimension  $D_k$  is a controllable parameter. The maximum value of  $\{D_k\}$  is denoted as the maximal bond dimension  $D_{\text{max}}$ . In practice, we systematically increase  $D_{\text{max}}$  until the converged and numerically exact results are obtained. Similarly, the super-Hamiltonian  $\mathcal{H}$  can be decomposed as the matrix product operator. For evolving Eq. (22), we employ a time propagation scheme based on the time-dependent variable principle, as described in Refs. 44–46.

### C. Observables

The rigorous expression to calculate quantum rate constants in the flux correlation function formalism has been well established.<sup>56–59</sup> For a single molecule with the symmetric double well potential as described in Sec. II A, we assume that the reactant and product region are separated by a diving surface at  $x_i^{\text{ds}} = 0$ . The population of the  $i$ th molecule in the product (right well) and the reactant (left well) region are obtained as

$$P_i^P(t) = \text{Tr} \{ h_i \rho(t) \} = \text{Tr}_{\text{sys}} \{ h_i \rho_{\text{sys}}(t) \} = \langle 1_{\text{sys}} | \hat{h}_i | \Psi^{\mathbf{n}=0}(t) \rangle, \quad (25a)$$

$$P_i^R(t) = \text{Tr} \{ (1 - h_i) \rho(t) \} = 1 - P_i^P(t). \quad (25b)$$

Here  $h_i = \theta(x_i - x_i^{\text{ds}})$  is the projection operator defined as a Heaviside function,  $|\Psi^{\mathbf{n}=0}(t)\rangle = |\mathbf{n} = \mathbf{0}\rangle |\Psi(t)\rangle$  is the reduced

wave function projecting all dissipative modes to the ground state. The unit system vector is defined as  $|1_{\text{sys}}\rangle = \otimes_i \sum_{s_i} |s_i s_i\rangle$  and can be decomposed in the MPS format as a tensor product

$$1_{\text{sys}} = I_{d_1} I'_{d_1} \cdots I_{d_{N_{\text{sys}}}} I'_{d_{N_{\text{sys}}}}, \quad (26)$$

where  $I_{d_i}$  is a rank-3 tensor with the size  $1 \times d_i \times d_i$  and the elements  $I_{d_i}^{[1,k,l]} = \delta_{kl}$ . Here,  $d_i$  is the number of states for the  $i$ th system DoF. The tensor  $I'_{d_i}$  is also a rank-3 tensor with the size  $d_i \times 1 \times d_i$  and the elements at  $I'_{d_i}^{[k,1,l]} = \delta_{kl}$ . The population dynamics of a specified state, such as the  $k$ th vibrationally excited state in the  $i$ th system DoF, is given by an inner product

$$P(v_{i,k}, t) = \left( \otimes_{j \neq i} \sum_{v_j} \langle v_j v_j | \right) \langle v_{i,k} v_{i,k} | \Psi^{\mathbf{n}=0}(t) \rangle \quad (27)$$

The forward reaction rate from the reactant region to the product region can be expressed as.<sup>57-59</sup>

$$k_i = \lim_{t \rightarrow t_p} k_i(t) = \lim_{t \rightarrow t_p} \frac{C_i^{\text{flux}}(t)}{2P_i^r(t) - 1}, \quad (28)$$

where  $t_p$  means the time at which  $k_i(t)$  reaches a plateau. The flux correlation function is defined as

$$C_i^{\text{flux}}(t) = -\frac{dP_i^r(t)}{dt} = \text{Tr}\{\rho_r(t) F_i\} = \langle 1_{\text{sys}} | \tilde{F}_i | \Psi^{\mathbf{n}=0}(t) \rangle, \quad (29)$$

where the flux operator is defined as  $F_i = i[H, h_i]$ . Note that, to obtain  $\rho_r(t)$  in Eq. (28) we employ the initial system density operator

$$\rho_{\text{sys}}(t=0) = \left( \prod_{i=1}^{N_{\text{mol}}} \frac{e^{-\frac{\beta H_{\text{mol},i}}{2}} (1-h_i) e^{-\frac{\beta H_{\text{mol},i}}{2}}}{Z_i} \right) \cdot \frac{e^{-\beta H_{\text{cav}}}}{\text{Tr}\{e^{-\beta H_{\text{cav}}}\}} \quad (30)$$

with  $Z_i = \text{Tr}_i \left\{ e^{-\frac{\beta H_{\text{mol},i}}{2}} (1-h_i) e^{-\frac{\beta H_{\text{mol},i}}{2}} \right\}$ . The singular value decomposition of the initial density matrix in Eq. (30) is employed to construct the initial matrix product state. Note that the plateau value of  $k_i(t)$  in Eq. (28), i.e. the reaction rate is not dependent on the initial density matrix assumed in Eqs. (11) and (30).

### III. RESULTS

In this section, we employ the method described above to investigate the cavity-induced rate modification in a symmetric double well model. We begin by outlining the model parameters and simulation details used in our calculations. Subsequently, to unravel the underlying reaction mechanisms, understand the role of the cavity mode, and assess the impact of molecular interactions, we analyze the results obtained for a series of models with an increasing number of DoFs and complexity.

TABLE I. Eigenenergies of the bare molecule for two different masses.

$\epsilon_k^{\text{mol}}$ (cm <sup>-1</sup> )	$\epsilon_0^{\text{mol}}$	$\epsilon_1^{\text{mol}}$	$\epsilon_2^{\text{mol}}$	$\epsilon_3^{\text{mol}}$	$\epsilon_4^{\text{mol}}$	$\epsilon_5^{\text{mol}}$
$M = 1$ a.u.	675	677	1818	1914	2617	3121
$M = 2$ a.u.	485	485	1382	1387	2079	2189

#### A. Simulation details

First, we provide the numerical details of the following calculations. To be consistent with the previous studies,<sup>30,33,37,38</sup> we adopt the same barrier parameters of the potential energy surface (PES) in Eq. (3), i.e.  $E_b = 2250$  cm<sup>-1</sup> and  $\omega_b = 1000$  cm<sup>-1</sup>. For the molecular dissipative bath, the characteristic frequency  $\Omega_i = 200$  cm<sup>-1</sup> and the reorganization energy  $\lambda_i = 0.05 \omega_b \Omega_i$  are used. The characteristic frequency for the cavity bath remains fixed at  $\Omega_c = 1000$  cm<sup>-1</sup> and we assume a cavity lifetime of  $\tau_c = \frac{2J_c(\omega_c)}{\omega_c(1-e^{-\beta\omega_c})} = 200$  fs. Thus, the reorganization energy  $\lambda_c$  is related to the cavity lifetime  $\tau_c$  and frequency  $\omega_c$  as given by

$$\lambda_c = \frac{(\omega_c^2 + \Omega_c^2)(1 - e^{-\beta\omega_c})}{4\Omega_c \tau_c}. \quad (31)$$

In this work, we adopt the Padé decomposition scheme<sup>54</sup> for the exponential expansion of the time correlation function in Eq. (17). The environment is thermalized at the ambient temperature  $T = 300$  K. A Padé pole number  $P = 3$  is found to be sufficient for obtaining the converged results throughout the simulations at this temperature. The convergence is meticulously verified concerning the hierarchical tier  $L_\alpha$ , the maximal bond dimension, and the time step. For each dissipative bath mode, the range of the occupation number  $n_{\alpha p}$  is defined by  $0 \leq n_{\alpha p} \leq L_\alpha$ . For simplicity, we take all  $L_\alpha$  to be the same and  $L = 10$  assures the convergence for the parameters given above. The maximal bond dimension used in this work is  $D_{\text{max}} = 60$ . It is worth noting that, in our experience, the MPS/TT decomposition along with the tangent-space time propagation scheme for evolving the HEOM in twin space (see Eq. (22)) always allows a significantly larger time step than directly solving Eq. (18) with a differential equation solver, such as Runge-Kutta integrator. For this work, we employ the time step  $\Delta t = 1$  fs.

The molecular Hamiltonian  $H_{\text{mol}}$  is described in a discrete variable representation<sup>60,61</sup> (DVR) with 500 grid points. The coordinate spans from  $x_i^{\text{min}} = -100$  a.u. to  $x_i^{\text{max}} = 100$  a.u. Further diagonalization of the molecular matrix in DVR representation, i.e.  $H_{\text{mol}}$ , yields the eigenenergies  $\{\epsilon_k^{\text{mol}}\}$  and eigenstates  $\{|v_k^{\text{mol}}\rangle\}$  of the bare molecule. The cavity photon mode is represented in harmonic eigenstates. The lowest  $N_v^{\text{mol}}$  molecular eigenstates and  $N_v^{\text{cav}}$  cavity photonic states are taken into account. The specific values of  $N_v^{\text{mol}}$  and  $N_v^{\text{cav}}$  used will be discussed in the subsequent sections.

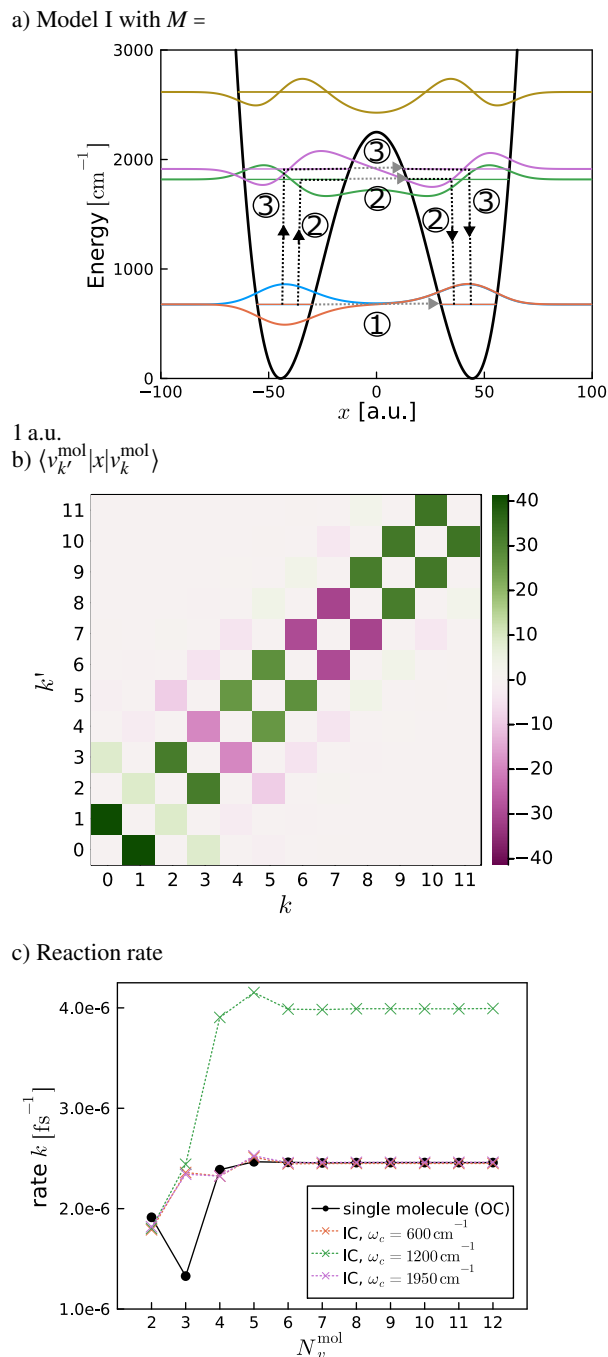


FIG. 2. a) Potential energy surface for a symmetric double well model. The colored horizontal lines indicate the eigenenergies of the bare molecule. The wavy lines represent various molecular vibrational eigenstates. Here, we take the molecular mass  $M = 1$  a.u. . b) Heatmap representation of the coordinate  $x$  in the molecular vibrational eigenstate representation. c) Reaction rate  $k$  as a function of the number of vibrational eigenstates  $N_v^{\text{mol}}$  taken in a simulation. The black solid line with circles is the results of a single molecule outside the cavity (OC). The colored dotted lines with crosses correspond to a single molecule inside the cavity (IC) for three different cavity frequencies.

## B. Single molecule outside cavity

To elucidate the physicochemical processes in reaction dynamics, we start by considering a single molecule placed outside an optical cavity with two different molecular masses,  $M = 1$  a.u. and  $M = 2$  a.u. . The lowest six eigenenergies of the bare molecule are listed in Table I.

First, we consider the effective molecular mass as  $M = 1$  a.u. , which is also used in the prior studies.<sup>30,37,38</sup> . In this case (Model I), there are four vibrational eigenstates below the barrier, as illustrated in Fig. 2(a). The transition between different vibrational eigenstates is caused by the solvent, represented by a bilinear system-bath interaction in Eq. (10). Thus, the transition probability between the states  $|v_k^{\text{mol}}\rangle$  and  $|v_{k'}^{\text{mol}}\rangle$  is dictated by  $\langle v_{k'}^{\text{mol}} | x | v_k^{\text{mol}} \rangle$ . The heatmap in Fig. 2(b) displays  $\langle v_{k'}^{\text{mol}} | x | v_k^{\text{mol}} \rangle$  in different vibrational states, and the values are also provided in the supplementary information (SI). Note that for an anharmonic system, transitions beyond the nearest neighboring levels are permitted.

To comprehend the underlying reaction mechanisms, we find it helpful to calculate the reaction rate  $k$  for an incremental  $N_v^{\text{mol}}$ , the number of the vibrational eigenstates considered in the simulation. The black line with solid circles in Fig. 2(c) shows the reaction rate  $k$  as a function of  $N_v^{\text{mol}}$ . When considering only the lowest two levels ( $N_v^{\text{mol}} = 2$ ), the reaction rate has a finite value,  $k = 2 \times 10^{-6} \text{ fs}^{-1}$ , which stems from the tunneling process, as illustrated by Path ① in Fig. 2(a). When the third level is included, the solvent can induce the vibrational transition between the states  $|v_1^{\text{mol}}\rangle$  and  $|v_2^{\text{mol}}\rangle$ , opening up a cotunneling pathway, Path ②, as exhibited in Fig. 2(a). Interestingly, we observe that the introduction of Path ② leads to a decreased reaction rate, which could be due to destructive interference with Path ①. The addition of the fourth state  $|v_3^{\text{mol}}\rangle$  introduces another cotunneling path, ③ as shown in Fig. 2(a) and leads to a net increase in the reaction rate. Notably, the rate for  $N_v^{\text{mol}} = 4$  is already close to the converged result obtained with  $N_v^{\text{mol}} > 6$ . Higher vibrational states above the barrier contribute minimally to the reaction. due to small transition probabilities (from the vibrational states  $|v_0^{\text{mol}}\rangle$  and  $|v_1^{\text{mol}}\rangle$ ) and negligibly low population probabilities. This can be seen from Fig. 5(a), where we display the population dynamics of different vibrational states.

Next, we investigate the case with the larger mass,  $M = 2$  a.u. , while keeping all other parameters fixed. In this scenario (Model II), the energy gaps between vibrational levels become narrower and the zero-point energy (the energy of the lowest two degenerate eigenstates) is shifted further away from the barrier (see Table I). As a consequence, there are six states below the energy barrier, as shown in Fig. 3(a). The tunneling rate for  $N_v^{\text{mol}} = 2$  is significantly reduced to  $1.5 \times 10^{-9} \text{ fs}^{-1}$ . The states  $|v_2^{\text{mol}}\rangle$  and  $|v_3^{\text{mol}}\rangle$  are nearly degenerate. However, while the inclusion of state  $|v_2^{\text{mol}}\rangle$  only slightly increases the reaction rate, the involvement of both, in great contrast, leads to a significant speedup by two orders of magnitude. The rate for  $N_v^{\text{mol}} = 4$  is  $1.9 \times 10^{-7} \text{ fs}^{-1}$ . Unlike Model I, we observe in Fig. 3(c) another notable leap in the reaction rate when the states  $|v_4^{\text{mol}}\rangle$  and  $|v_5^{\text{mol}}\rangle$  are also

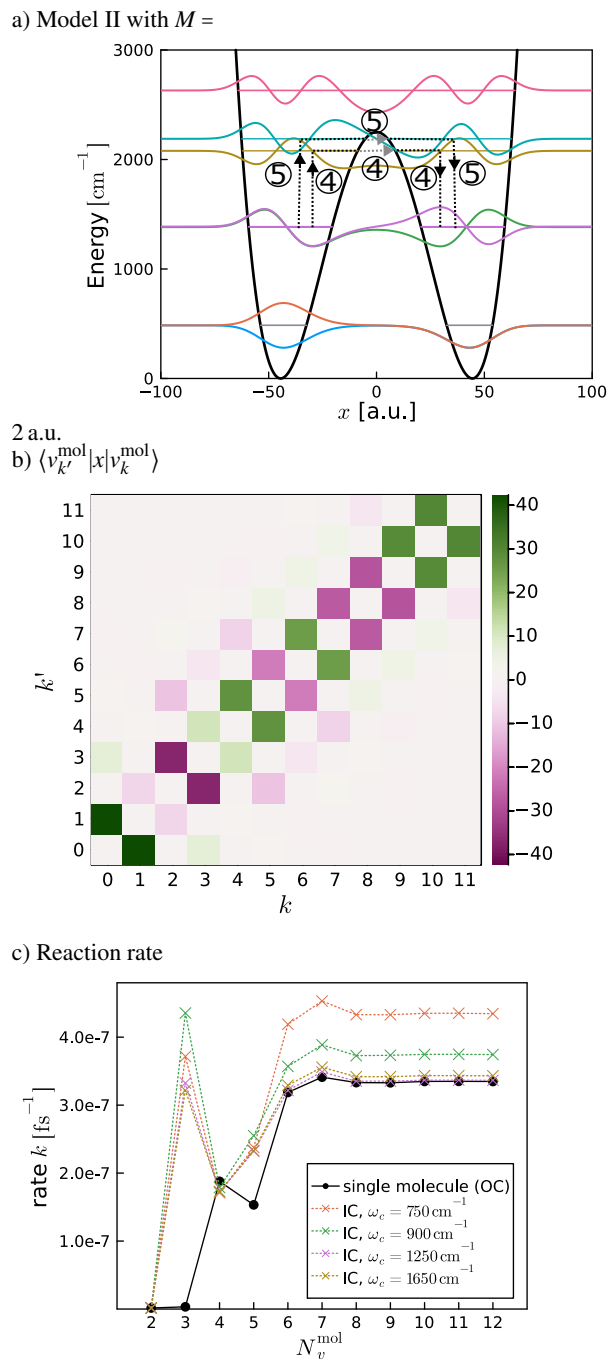


FIG. 3. Same as Fig. 2 expect that the molecular mass is  $M = 2 \text{ a.u.}$

included. This is due to two extra cotunneling paths, ④ and ⑤, as shown in Fig. 3(a). Path ④ comprises a pair of solvent-induced vibrational excitation and relaxation between the states  $|v_3^{\text{mol}}\rangle \leftrightarrow |v_4^{\text{mol}}\rangle$ , which is allowed by symmetry (see Fig. 3(b)), as well as the shallow tunneling at the near-barrier vibrational state  $|v_4^{\text{mol}}\rangle$ . Similarly, Path ⑤ is a cotunneling process that involves the vibrational transition  $|v_2^{\text{mol}}\rangle \leftrightarrow |v_5^{\text{mol}}\rangle$  and the tunneling at  $|v_5^{\text{mol}}\rangle$ . The reaction rate converges when at least the lowest eight eigenstates are considered, and the interference between all possible reaction paths results in a

rate  $k = 3.3 \times 10^{-7} \text{ fs}^{-1}$ , which is six times smaller than that of Model I.

In summary, for a double-well system outside the cavity, the reaction takes place through the tunneling at the lowest two vibrational levels and a number of cotunneling processes. Each cotunneling process involves a pair of solvent-induced vibrational excitation and relaxation, bridged by the tunneling at the vibrationally excited state. The reaction rate is not solely determined by summing up these reaction pathways but also by their interference. For Model I with a much smaller molecule-solvent interaction strength  $\lambda_i$ , or in some other system as demonstrated in Appendix A, it is interesting to note that including all cotunneling processes eventually decreases the reaction rate.

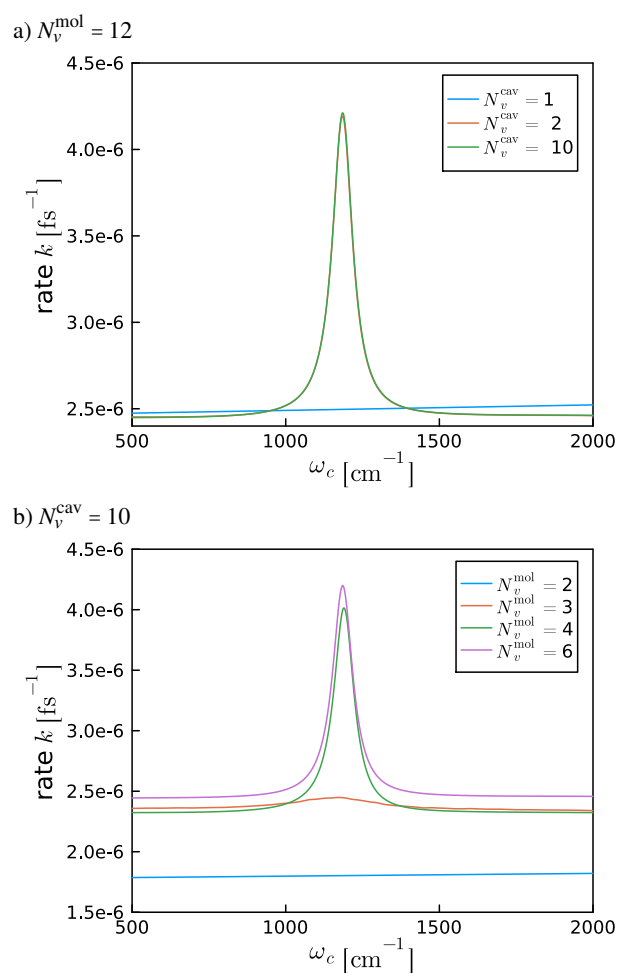


FIG. 4. Reaction rate  $k$  as a function of the cavity frequency  $\omega_c$  for Model I. In panel (a), we set  $N_v^{\text{mol}} = 12$  and explore a varying number of  $N_v^{\text{cav}}$ , i.e. considering the lowest  $N_v^{\text{cav}}$  states for the cavity mode. In panel (b), we fix  $N_v^{\text{cav}} = 10$  and explore a varying number of  $N_v^{\text{mol}}$ , i.e. considering the lowest  $N_v^{\text{mol}}$  eigenstates for the molecular vibrational mode.

### C. Single molecule inside cavity

To elucidate the impact of the cavity photon mode on reaction dynamics, we place a single molecule inside an optical cavity and vary the cavity photon frequency. Additionally, we assume that the molecular transition dipole moment is a function of the reaction coordinate and aligned in the same direction as the light polarization, i.e.  $\vec{\mu}(x) \cdot \vec{e} = x$ .

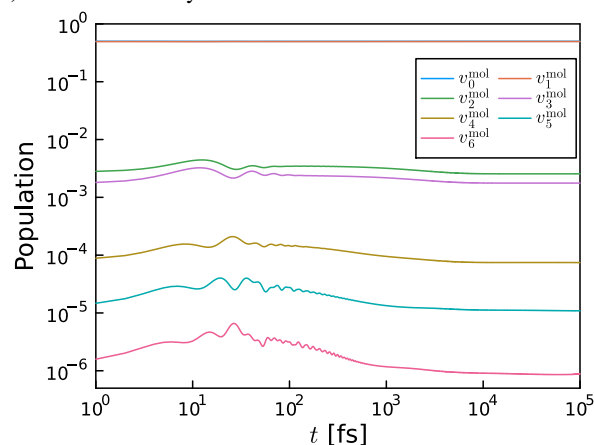
Once again, we commence our analysis with Model I, considering a mass of  $M = 1$  a.u. and a light-matter interaction strength  $\eta_c = 0.00125$ . To gain a deeper understanding of the molecular reaction dynamics within the cavity, we first set  $N_v^{\text{mol}} = 12$  and calculate the reaction rate across a cavity frequency range for varying  $N_v^{\text{cav}}$ . Subsequently, while maintaining  $N_v^{\text{cav}} = 10$ , we explore the rate profile,  $k$  versus  $\omega_c$  with different  $N_v^{\text{mol}}$ . The results are presented in Fig. 4. Furthermore, for a direct comparison with the reaction occurring outside the cavity, we illustrate in Fig. 2(c) the dependence of the rate on  $N_v^{\text{mol}}$  for reactions inside the cavity with three distinct cavity frequencies.

We observed that including either only the photonic ground state ( $N_v^{\text{cav}} = 1$ ) or the lowest two molecular vibrational states ( $N_v^{\text{mol}} = 2$ ), the reaction rate  $k$  increases slightly and linearly with  $\omega_c$ . This increase stems from the change in the dipole self-energy term  $\omega_c \eta_c^2 x^2$  in Eq. (5), which is necessary to have a gauge invariant Hamiltonian and crucial for an accurate description of light-matter interactions under the dipole gauge.<sup>62</sup> The absence of a peak confirms that the zero-point energy effect of both the cavity photonic and the molecular DoF is irrelevant for the resonance structure in the cavity frequency-dependent rate profile. This finding aligns with Ref. 30, which demonstrates that, despite the improvement of the ring-polymer molecular dynamics over the classical treatment due to accounting for the zero-point energy effect, it is not sufficient for studying chemical reactions inside the cavity.

On the photonic side, a sharp peak centered at  $\omega_c = 1185 \text{ cm}^{-1}$  emerges when the first photonic excited state  $|v_1^{\text{cav}}\rangle$  is included. This suggests that the rate modification inside the cavity is associated with the absorption or emission of one cavity photon. On the molecular side, a small peak in the rate profile is observed with  $N_v^{\text{mol}} = 3$ . Intriguingly, different from the reaction outside the cavity, the reaction rate for  $N_v^{\text{mol}} = 3$  is larger than that for  $N_v^{\text{mol}} = 2$  over the entire  $\omega_c$  range. This indicates that the presence of the cavity mode itself, even in the off-resonant condition, can alter the interference pattern between Path ① and ② shown in Fig. 2(a). The peak becomes significantly stronger and sharper with the inclusion of the vibrational state  $|v_3^{\text{mol}}\rangle$  ( $N_v^{\text{mol}} = 4$ ). Convergence is achieved when  $N_v^{\text{mol}} > 6$ . This clearly indicates that the vibrationally excited states and tunneling are involved in cavity-induced rate enhancement.

We also compared the population dynamics of different vibrational states outside and inside a resonant cavity, as shown in Fig. 5. For the molecule outside the cavity, after a transient fluctuation due to the establishment of the molecule-solvent entanglement, the population in various states reaches a steady distribution in the long-time regime, where the flux-side correlation function plateaus. Placing the molecule inside a res-

a) Outside the cavity



b) Inside the cavity ( $\omega_c = 1200 \text{ cm}^{-1}$ )

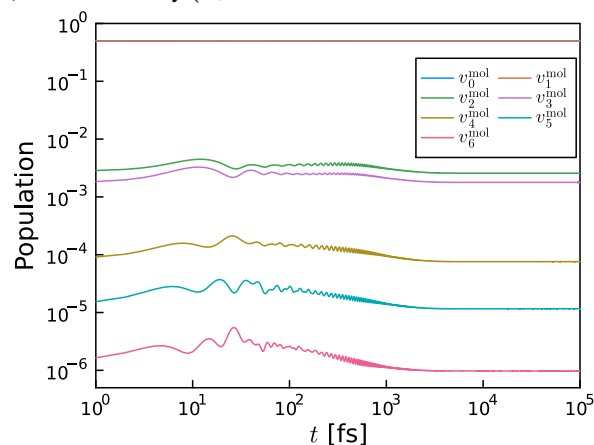


FIG. 5. Population dynamics of the lowest seven vibrational eigenstates for a single molecule outside (a) and inside the optical cavity (b). The results are obtained with  $N_v^{\text{mol}} = 12$  and  $N_v^{\text{cav}} = 10$ . The majority of the population remains in the lowest two vibrational states, with the result for  $|v_0^{\text{mol}}\rangle$  overlaid by that for  $|v_1^{\text{mol}}\rangle$ .

onant cavity leads to a strong oscillation in the intermediate time period ( $100 \text{ fs} < t < 1000 \text{ fs}$ ). The long-time population is unaffected by the cavity mode.

Furthermore, we found that the resonance structure in the rate profile disappears when the coupling of the cavity mode to the cavity photon bath is turned off, in agreement with the discussion in Ref. 37. This indicates that the cavity bath also plays an indispensable role in cavity-induced rate modification. In addition, all the above results remain unchanged when the molecular dipole moment is pointed in the opposite direction of the light polarization, i.e.  $\vec{\mu}(x) \cdot \vec{e} = -x$ . The ratio  $k/k_0$  ( $k$  is the rate in the resonant condition and  $k_0$  is the reaction rate outside the cavity) is almost quadratic to the light-matter interaction strength  $\eta_c$ , as found in Ref. 38. This implies that the cavity-induced rate enhancement is caused by a second-order process with respect to the light-matter interaction, i.e.  $(k - k_0)/k_0 \propto (\eta_c \vec{\mu}(x) \cdot \vec{e})^2$ .

Bringing together all the pieces of the puzzle mentioned above, we propose a reaction mechanism that can well explain

the appearance of the resonance, that is, the rate increases most pronouncedly when the cavity frequency is in the vicinity of the molecular vibrational frequency. This increase is attributed to a cavity-induced cotunneling process, as illustrated in Fig. 6(a), which is analogous to but more complicated than the solvent-induced cotunneling process.

When  $\omega_c = 1185\text{cm}^{-1}$ , the emission of a photon can promote two molecular vibrational transitions (due to the broadening effect caused by the environment):  $v_1^{\text{mol}} \rightarrow v_2^{\text{mol}}$  with an energy difference  $\Delta\varepsilon_{1\rightarrow 2}^{\text{mol}} = 1140\text{cm}^{-1}$  and  $v_0^{\text{mol}} \rightarrow v_3^{\text{mol}}$  with  $\Delta\varepsilon_{0\rightarrow 3}^{\text{mol}} = 1238\text{cm}^{-1}$ , as shown by the blue-shaded region in Fig. 6(a). Simultaneously, the cavity mode is thermalized by its coupling to the cavity photon bath, and the molecular wave packet quickly tunnels to the right well on the vibrationally excited states. Subsequently, the relaxation from the vibrationally excited state to the low-lying state ( $v_2^{\text{mol}} \rightarrow v_1^{\text{mol}}$  and  $v_3^{\text{mol}} \rightarrow v_0^{\text{mol}}$ ) in the product region excites a photon in the cavity mode, which then leaks to the cavity bath, as shown in the yellow-shaded area in Fig. 6(a). Therefore, the molecular vibrational heating/cooling is energetically fueled by the cavity photon bath through the mediation of a resonant cavity mode. After a cavity-induced cotunneling process is accomplished, the population of different vibrational levels remains the same. If this additional reaction channel interferes constructively with other pathways in Fig. 2(a), the reaction rate is increased.

Under off-resonant conditions, the energy exchange between the cavity mode and molecular vibration is either energetically not allowed or kinetically ineffective. For instance, when  $\omega_c = 600\text{cm}^{-1}$ , a molecular transition necessitates the simultaneous emission of two photons, as depicted in Fig. 6(b), which has a low probability of occurrence. Consequently, the reaction rate undergoes a minimal change. In the high  $\omega_c$  region, such as  $\omega_c = 1950\text{cm}^{-1}$ , the photon energy is close to the transition energy between  $v_1^{\text{mol}} \leftrightarrow v_4^{\text{mol}}$  as shown in Fig. 6(c). Nevertheless, this vibrational transition is impeded by its low transition probability, governed by  $\langle v_4^{\text{mol}} | x | v_1^{\text{mol}} \rangle$ . Additionally, the population in the photonic excited state diminishes with increasing  $\omega_c$ , which is shown in the SI.

In short, the peak in the photon frequency-dependent rate profile results from a combined effect of energetic and kinetic factors. Firstly, the photon frequency should match a vibrational transition energy to enable the exchange of energy between the molecular vibration and the cavity mode. The broadening of the peak is determined by the system-environment coupling strength. Secondly, the molecular vibrational transition should be both kinetically allowed and efficient. Thirdly, the cavity photon bath also plays a crucial role in thermalizing the cavity mode, and this process is likely to be most efficient when the characteristic frequency resonates with the cavity photon frequency. This provides a possible explanation for an observation noted in a prior study<sup>38</sup>, wherein the reaction rate inside a resonant cavity exhibits a turnover when increasing the cavity lifetime  $\tau_c$ . We should also emphasize that when multiple reaction pathways exist, neglecting the inference between these paths cannot correctly predict the reaction rate.

In a recent work,<sup>33</sup> a variety of mixed quantum-classical

approaches are employed to investigate the resonance behavior of the cavity frequency-dependent rate profile. Specifically, the reaction coordinate is treated quantum mechanically, while other DoFs are treated classically. They found that although these mixed quantum-classical methods can capture the shape resonance of the cavity-modified reaction rate, both the reaction rate  $k_0$  outside the cavity and the ratio  $k/k_0$  inside the cavity are significantly overestimated. This could be attributed to the missing phase factor in the classically treated part.

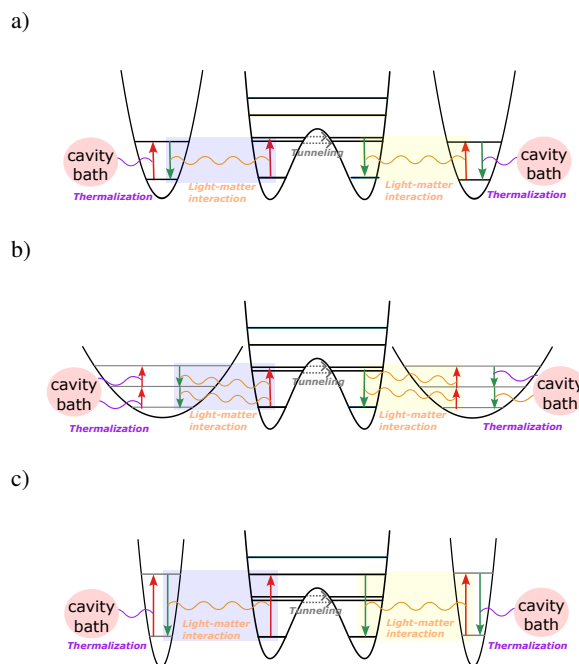


FIG. 6. Schematic representation of the cavity-induced cotunneling pathway and the mechanism underlying the resonance structure in the rate profile. In panel (a), we showcase the resonant condition, where the cavity photon frequency  $\omega_c$  is in close resonance with the molecular vibrational transition energy. Panel b) illustrates a condition in the low cavity frequency regime, where the molecular vibrational transition requires the simultaneous emission of two photons. Panel c) exhibits another condition in the high cavity frequency regime, where a cavity photon excites the molecule to a higher vibrationally excited state. Furthermore, the cavity bath facilitates the influx and efflux of photons from the cavity mode.

For an anharmonic system, the transition energy varies between different vibrational levels. In principle, we can observe multiple peaks in the cavity frequency-dependent rate profile, as long as multiple vibrational transitions meet the aforementioned energetic and kinetic criteria. This is the case for Model II with  $M = 2$  a.u. Fig. 7 displays the cavity frequency-dependent rate profile with the light-matter interaction strength  $\eta_c = 0.00125$  for different  $N_v^{\text{cav}}$  in panel (a) and different  $N_v^{\text{mol}}$  in panel (b). Additionally, the rates as a function of  $N_v^{\text{mol}}$  for four different cavity photon frequencies are shown in Fig. 3(c).

Again, no peak is observed when  $N_v^{\text{cav}} = 1$  or  $N_v^{\text{mol}} = 2$  (data not shown), and in this case, the reaction rate increases

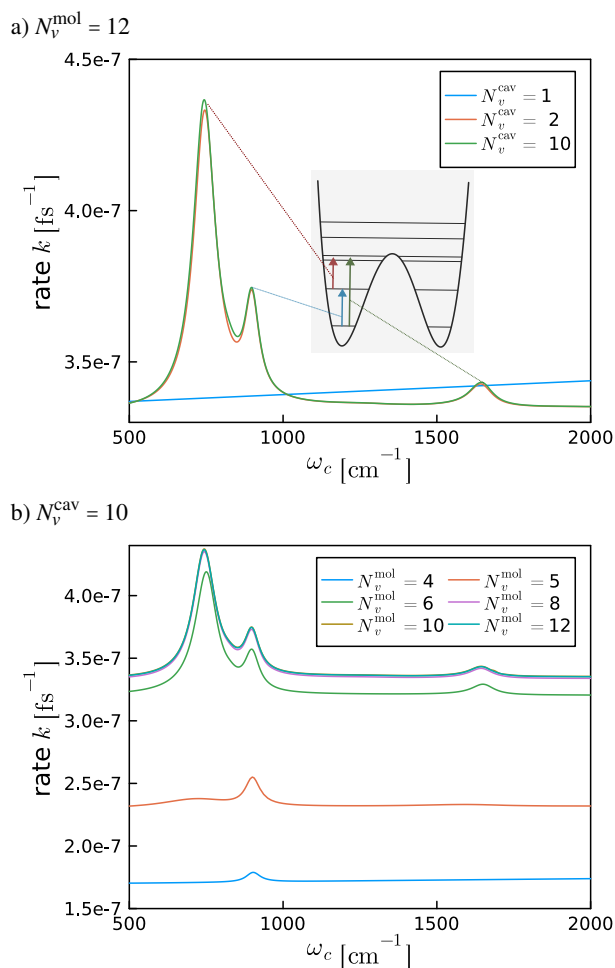


FIG. 7. Same as Fig. 4 expect that  $M = 2$  a.u. .

slightly with  $\omega_c$ , due to the larger dipole self-energy,  $\omega_c \eta_c^2 x^2$ . Full convergence requires  $N_v^{\text{cav}} > 3$ . However, the data for  $N_v^{\text{cav}} = 2$  have already captured the key feature in the rate profile, which exhibits three sharp peaks, centered at around  $745 \text{ cm}^{-1}$ ,  $900 \text{ cm}^{-1}$ , and  $1645 \text{ cm}^{-1}$ , respectively.

To explore the origin of these three peaks, we fixed  $N_v^{\text{cav}} = 10$  and analyzed the rate profile  $k$  as a function of  $\omega_c$  with different  $N_v^{\text{mol}}$ . When  $N_v^{\text{mol}} = 4$ , the peak centered at  $\omega_c = 900 \text{ cm}^{-1}$  arises, which matches the energy gap  $\Delta \epsilon_{0 \leftrightarrow 3}^{\text{mol}} = 902 \text{ cm}^{-1}$  for the transition  $v_0^{\text{mol}} \leftrightarrow v_3^{\text{mol}}$  and  $\Delta \epsilon_{1 \leftrightarrow 2}^{\text{mol}} = 897 \text{ cm}^{-1}$  for  $v_1^{\text{mol}} \leftrightarrow v_2^{\text{mol}}$ . Two other peaks around  $745 \text{ cm}^{-1}$  and  $1645 \text{ cm}^{-1}$  start to emerge when the fourth vibrational level is included ( $N_v^{\text{mol}} = 5$ ), and become much more apparent for  $N_v^{\text{mol}} = 6$ , as shown in Fig. 7(b). The strongest peak centered at  $745 \text{ cm}^{-1}$  is related to the transition  $v_3^{\text{mol}} \leftrightarrow v_4^{\text{mol}}$  with  $\Delta \epsilon_{3 \leftrightarrow 4}^{\text{mol}} = 691 \text{ cm}^{-1}$  and  $v_2^{\text{mol}} \leftrightarrow v_5^{\text{mol}}$  with  $\Delta \epsilon_{2 \leftrightarrow 5}^{\text{mol}} = 806 \text{ cm}^{-1}$ . The peak in the high-frequency regime can be assigned to the transition  $v_1^{\text{mol}} \leftrightarrow v_4^{\text{mol}}$  with  $\Delta \epsilon_{1 \leftrightarrow 4}^{\text{mol}} = 1593 \text{ cm}^{-1}$  and  $v_0^{\text{mol}} \leftrightarrow v_5^{\text{mol}}$  with  $\Delta \epsilon_{0 \leftrightarrow 5}^{\text{mol}} = 1704 \text{ cm}^{-1}$ , and it appears owing to the fast tunneling near the barrier top. Convergence is basically achieved when  $N_v^{\text{mol}} > 8$ , which means that higher vibrational levels barely contribute to the rate promotion.

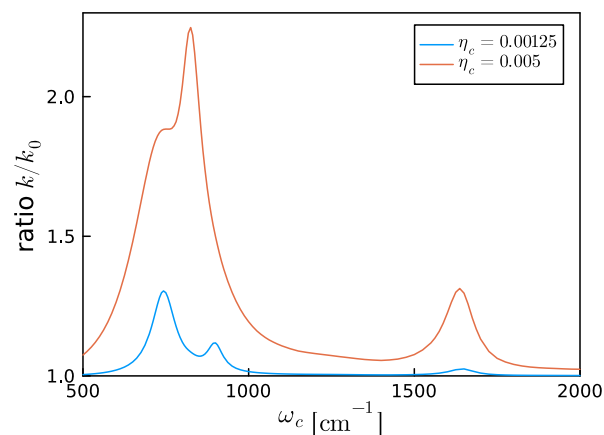


FIG. 8. Rate modification profile  $k/k_0$  as a function of the cavity frequency  $\omega_c$  for Model II with two different light-matter interaction strengths  $\eta_c$ . Here  $k_0$  denotes the reaction rate of a single molecule outside the cavity. The results are obtained with  $N_v^{\text{cav}} = 10$  and  $N_v^{\text{mol}} = 12$ .

It is noteworthy that when  $N_v^{\text{mol}} = 3$ , the rates inside the cavity are many orders of magnitude larger than that outside cavity, as shown in Fig. 3(c). Conversely, for  $N_v^{\text{mol}} = 4$ , the rates across the entire frequency regime are slightly smaller compared to the rate outside the cavity. This highlights the intricate role of path interference between the cavity-induced cotunneling channels and other reaction paths depicted in Fig. 3(a). A more comprehensive exploration in this direction remains a subject in future investigations.

We also explored the reaction at a larger light-matter interaction strength,  $\eta_c = 0.005$ . A detailed analysis of the reaction dynamics is presented in the SI. A larger  $\eta_c$  entails considering more highly excited photonic states (e.g.  $N_v^{\text{cav}} > 6$  for  $\eta_c = 0.005$ ) to obtain accurate results. The reaction rates exhibit a significant increase across the entire frequency range, as depicted in Fig. 8, which displays the ratio  $k/k_0$  as a function of  $\omega_c$ . Additionally, we observe that the relative heights of two lower-frequency peaks are changed. The most prominent peak now appears at  $825 \text{ cm}^{-1}$  with a shoulder around  $750 \text{ cm}^{-1}$ . This shift is attributed to the stronger coupling to the cavity photon mode and successively to the cavity bath, resulting in a further broadening of molecular vibrational levels. As a consequence, a cavity photon with a frequency  $825 \text{ cm}^{-1}$  can induce both the vibrational transitions  $v_{0/1}^{\text{mol}} \leftrightarrow v_{3/2}^{\text{mol}}$  as well as  $v_{2/3}^{\text{mol}} \leftrightarrow v_{5/4}^{\text{mol}}$ , and thereby maximizes the rate enhancement. In other words, a stronger light-matter interaction can amalgamate nearby peaks corresponding to different vibrational transitions in an anharmonic system and intensify the rate modification.

As a side note, it is important to note that not all cavity-induced cotunneling pathways necessarily manifest as peaks in the cavity frequency-dependent rate profile. If the tunneling component of a cavity-induced cotunneling pathway is considerably slower than the reaction rate outside the cavity, a corresponding feature may not be observable in the rate pro-

file. An illustrative example is provided in Appendix B.

#### D. Two molecules inside cavity

To explore the influence of collective effects and molecular interactions on the reaction dynamics, we extend our investigation to include two molecules inside the cavity mode. These two molecules can interact indirectly by simultaneously coupling to the same cavity mode or directly by inter-molecular dipole-dipole interaction, denoted as  $\Delta_{12} = \Delta$  (see Eq. (2)). We begin by examining a homodimer, where both molecules are identical, and subsequently, a heterodimer with different masses. Additionally, we account for the dipole orientation effect in two configurations: parallel (para) and anti-parallel (anti-para). In the parallel configuration, the dipoles of both molecules align in the same direction as the light polarization  $\vec{e}$ . In the anti-parallel configuration, one molecular dipole aligns with the light polarization, i.e.  $\vec{\mu}_1(x_1) \cdot \vec{e} = x_1$ , while the other points in the opposite direction,  $\vec{\mu}_2(x_2) \cdot \vec{e} = -x_2$ , as illustrated in Fig. 9(a).

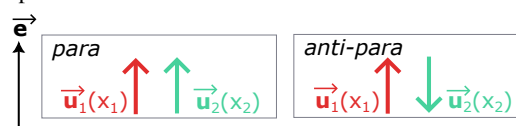
##### 1. Homodimer

We first consider a homodimer model, where the masses of both molecules are  $M_1 = M_2 = 1$  a.u., and the inter-molecular coupling is turned off, i.e.  $\Delta = 0$ . However, the molecules are indirectly coupled to each other through their mutual coupling to the cavity mode.

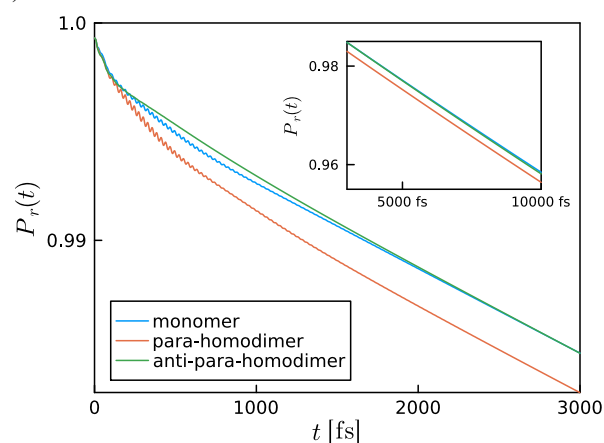
The dynamics of two molecules inside the cavity are basically identical to each other. In Fig. 9(b) and (c), we present the reactant population dynamics  $P_r(t) = P_r^1(t) = P_r^2(t)$ , and the scaled flux-side correlation function  $k(t) = k_1(t) = k_2(t)$  (see the definition in Eq. (28)), respectively, for para (orange lines) and anti-para (green lines) dipole configuration. The cavity frequency is set to  $\omega_c = 1200\text{cm}^{-1}$  and the light-matter coupling is  $\eta_c = 0.00125$ . For comparison, we also display the results for a single molecule inside the cavity (blue lines). The dipole orientation of two molecules has a strong impact on the transient dynamics. In the time regime  $t < 2000$  fs, we observe that for the para homodimer,  $P_r(t)$  decreases faster, and  $k(t)$  is more oscillatory as compared to those of the single molecule inside the cavity. Conversely, the opposite behavior is observed for the anti-para homodimer. However, the rate constant  $k$  obtained in the long time region when  $k(t)$  reaches the plateau is the same for both dipole configurations, which is slightly higher than that for the single molecule, as shown in the inset of Fig. 9(c).

In Fig. 10, we compare the rate profile,  $k/k_0$  against  $\omega_c$  of the homodimer in both orientations to that of a single molecule inside the cavity. Here,  $k_0$  is the reaction rate of a single molecule outside the cavity. The panels (a) and (b) correspond to the light-matter interaction  $\eta_c = 0.00125$  and  $\eta_c = 0.005$ , respectively. Although the rate is further increased due to the collective effect in both cases, it is only significant when the light-matter coupling is stronger. Over the entire

##### a) Dipole orientation



##### b)



##### c)

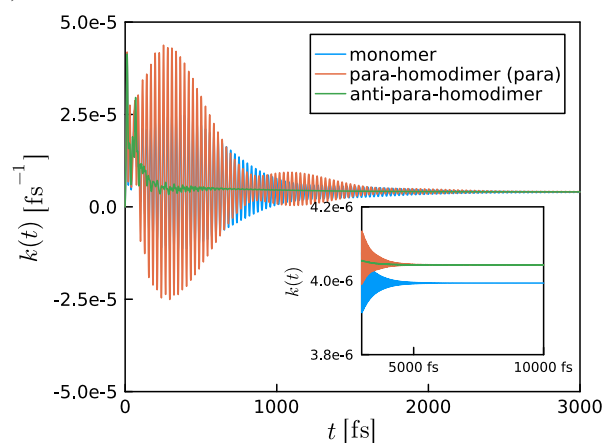


FIG. 9. a) Schematic illustration of the para and anti-para configurations of two molecular transition dipole moments. The arrow  $\vec{e}$  denotes the light polarization direction. b) Population dynamics of the reactant (in the left-well region) for a single molecule inside the cavity (blue), para-homodimer (orange) as well as anti-para-homodimer (green) inside the cavity. The photon frequency is  $\omega_c = 1200\text{cm}^{-1}$  and the light-matter interaction  $\eta_c = 0.00125$ . c) Scaled flux-correlation function  $k(t)$  for these three models. The insets in (b) and (c) display the corresponding dynamics in the longer time regime, where the reaction rate is extracted.

frequency regime, this collective effect-induced rate enhancement is independent of whether the dimer is in the para and anti-para dipole configuration.

The additional increase in the rate for a homodimer can be explained by an additional inter-molecular reaction channel, as illustrated in Fig. 11(a). When the first molecule is vibrationally excited and tunnels into the right well, the subsequent vibrational relaxation can induce the creation of one photon in the cavity mode, due to the light-matter interaction. Then,

the loss of the photon is coupled to the vibrational heating of the second molecule in the reactant region. The reverse process can also occur, where the first molecule in the reaction region is vibrationally heated and the second molecule in the product region is cooled down, through the intermediation of the cavity mode. Overall, the reaction rates of both molecules are increased. This intermolecular reaction channel involves four energy exchange processes between two molecules and the cavity photon mode. In other words, this rate enhancement is quartic to the light-matter interaction and scales like  $\sim \eta_c^4 (\mu_1(x_1) \cdot \vec{e})^2 (\mu_2(x_2) \cdot \vec{e})^2$ . Therefore, the rate enhancement effect is not obvious when  $\eta_c$  is small, as shown in Fig. 10(a). But after increasing the light-matter coupling to  $\eta_c = 0.005$ , we can observe a more distinct rate increase of a homodimer, compared to the single molecule inside the cavity, as shown in Fig. 10(b). It is important to note that, in experiments, a truly macroscopic number of molecules are collectively coupled to multiple cavity modes. As such, numerous intermolecular reaction pathways could exist between any pair of molecules and their commonly coupled cavity mode. This situation could potentially result in a remarkable increase in the reaction rate. Furthermore, the above results also suggest that the rate enhancement induced by this collective effect is quadratic to  $\vec{\mu}(x) \cdot \vec{e}$ , which indicates that it can survive in an isotropically disordered system.

So far, we only consider an indirect coupling of the molecules to each other. Now, we also include a direct intermolecular dipolar coupling term. Fig. 12 shows the rate  $k$  as a function of the intermolecular dipolar coupling  $\Delta$  for a homodimer outside (black lines) and inside (colored lines) the cavity with three different photon frequencies. The results for the para dipole configuration are displayed as the solid lines and those for the anti-para configuration as the dotted lines. For the dimer outside the cavity, the reaction rate increases with  $\Delta$  in the para dipole configuration, and decreases almost symmetrically with  $\Delta$  in the anti-para configuration. The dependence of the rate on  $\Delta$  is not changed in an off-resonant cavity (see the results for  $\omega_c = 800$  and  $1200 \text{ cm}^{-1}$ ). In the resonant condition, for the para configuration, the rate is first increased with  $\Delta$  and then saturates. But for the anti-para dipole configuration, the rate drops quickly with an increasing  $\Delta$ . Despite the opposite trends in the para and anti-para dimer, the rate modification effect is asymmetric in the resonant condition for two dipole orientations, as shown in Fig. 12. Therefore, we anticipate that the rate modification resulting from the direct intermolecular dipolar interaction may not be completely averaged out in a randomly oriented ensemble.

## 2. Heterodimer

Next, we consider a heterodimer in which two molecules have different masses. We choose  $M_1 = 1$  a.u. and  $M_2 = 2$  a.u. because, as shown in Figs. 4 and 7, these two molecules do not exhibit an overlap in the resonant peaks of the cavity frequency-dependent rate profile.

Fig. 13(a) presents the ratio  $k_1/k_{1,0}$  as a function of the cavity frequency  $\omega_c$  for the first molecule of the heterodimer in a

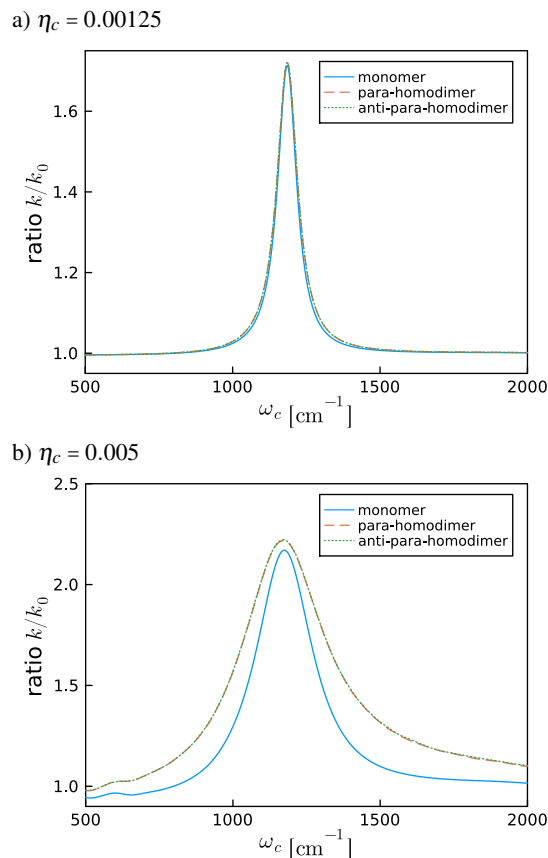


FIG. 10. Rate modification profile  $k/k_0$  as a function of the cavity frequency  $\omega_c$  with the light-matter interaction strength  $\eta_c = 0.00125$  (a) and  $\eta_c = 0.005$  (b) for a single molecule inside the cavity (blue), para-homodimer (orange) as well as anti-para-homodimer (green) inside the cavity. The results are obtained with  $N_v^{\text{cav}} = 10$  and  $N_v^{\text{mol}} = 12$ .

para dipole configuration inside the cavity. Fig. 13(b) is for the second molecule. A stronger light-matter coupling  $\eta_c = 0.005$  is employed in this context. For comparison, the results of the corresponding single molecule inside the cavity are depicted as dotted lines in Fig. 13. In contrast to the homodimer (see Fig. 10(b)), the reaction rates of two different molecules simultaneously coupled to the same cavity mode exhibit little change, as compared to the single molecule inside the cavity. This is because the reaction channel shown in Fig. 11(a) is no longer feasible in a heterodimer. To understand this, we can take a cavity mode with  $\omega_c = 1200 \text{ cm}^{-1}$  as an example. While the absorption of a photon is coupled to the emission of a phonon in the first molecule, the simultaneous emission of a photon can't excite the second molecule due to the energy mismatch, as illustrated in Fig. 11(b). Similarly, the vibrational transition in the second molecule  $v_1^{\text{mol}} \rightarrow v_2^{\text{mol}}$  is energetically resonant with a cavity mode of the frequency  $\omega_c = 750 \text{ cm}^{-1}$ , which is nevertheless off-resonant with the vibrational transitions in the first molecule, as illustrated in Fig. 11(c).

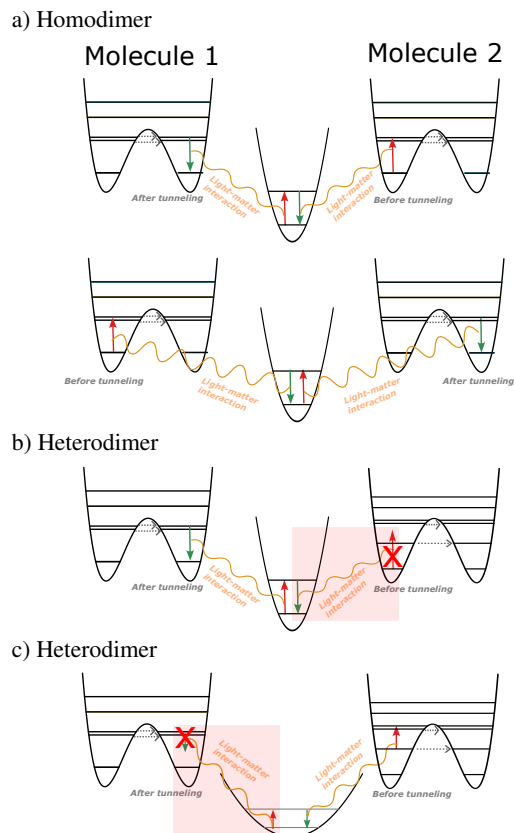


FIG. 11. a) Schematic illustration of an intermolecular reaction channel between two identical molecules through the mediation by the resonant cavity mode. Panels b) and c) demonstrate that the intermolecular reaction channel is inhibited in a heterodimer.

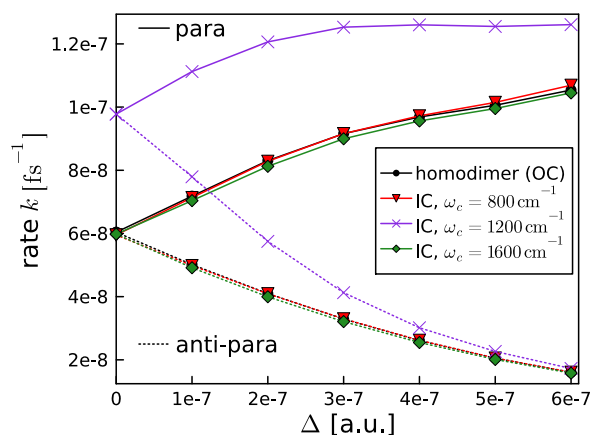


FIG. 12. Reaction rate  $k$  as a function of the intermolecular dipolar coupling  $\Delta$  for a homodimer outside (OC) and inside the cavity (IC) with three different cavity frequencies. The light-matter interaction strength is  $\eta_c = 0.00125$ . The solid and dotted lines correspond to the para and anti-para dipole configuration, respectively.

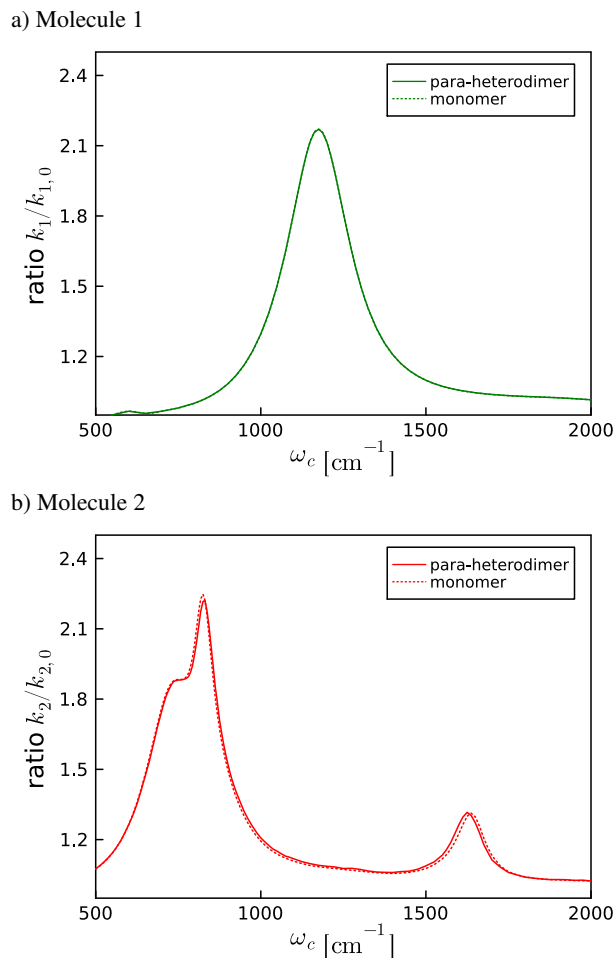


FIG. 13. Rate modification profile  $k_i/k_{i,0}$  of the  $i$ th molecule in a heterodimer as a function of the cavity frequency  $\omega_c$ . Panel (a) and (b) correspond to the first molecule with the mass  $M = 1$  a.u. and the second molecule with the mass  $M = 2$  a.u., respectively.  $k_{i,0}$  and  $k_{2,0}$  is the reaction rate of a single molecule outside the cavity. The dotted lines are the results for a single molecule inside the cavity (monomer). The light-matter interaction strength is set to  $\eta_c = 0.005$ . The results are obtained with  $N_V^{\text{cav}} = 10$  and  $N_V^{\text{mol}} = 12$ .

#### IV. CONCLUSION

In this work, we present a systematic theoretical investigation of condensed-phase chemical reactions both inside and outside an optical cavity. Our primary goal is to shed light on the mechanisms underlying cavity-induced modification in the reaction rate. To achieve this, our study employs a double-well description of molecular potential and utilizes an efficient, numerically exact open quantum system approach that combines the HEOM method with the MPS/TT formalism. This approach treats all DoFs quantum mechanically and, crucially, allows us to go beyond the single-molecule limit. Thereby, we also investigate the influence of collective effects, where two molecules are simultaneously coupled to the same cavity mode and they can also interact with each other in a direct dipole-dipole interaction, on the reaction rate.

Our numerical simulations, based on a single molecule, reveal that the sharp resonance structure in the cavity frequency-dependent rate profile is the combined effect of energetic and kinetic constraints. The energetic constraint stipulates that the energy of a photon  $\omega_c$  should match the energy gap of a vibrational transition from state  $v_k^{\text{mol}}$  to the other state  $v_{k'}^{\text{mol}}$ . The height of the resonance peak at  $\omega_c = \Delta\epsilon_{k \rightarrow k'}^{\text{mol}}$  is determined by kinetic factors, including the transition probability dictated by  $\langle v_k^{\text{mol}} | \mu(x) | v_{k'}^{\text{mol}} \rangle$ , the population probability, and the tunneling rate at these two vibrational states. When the cavity frequency is tuned to such a value, the cavity photon mode, along with the coupled cavity bath, induces vibrational heating in the reactant region and cooling in the product region. These pair of vibrational transitions, bridged by the tunneling in the vibrationally excited state, form a cavity-induced intramolecular cotunneling pathway. Depending on the interference of this reaction pathway with other reaction channels in the molecule, the rate is modified. Importantly, in highly anharmonic systems, our study predicts the possibility of observing multiple resonance peaks, where the aforementioned kinetic factors corresponding to these vibrational transitions are not exponentially suppressed.

To gain insight into the collective effect, i.e. when many molecules are simultaneously coupled to the cavity radiation mode, we go beyond the single molecule limit and consider two molecules inside the cavity. Our studies reveal that an additional intermolecular reaction pathway, involving two identical molecules and the resonant cavity mode, can further increase the reaction rate, compared to a single molecule inside the cavity. Furthermore, our results suggest that both the cavity-induced intra and intermolecular cotunneling process can persist in an isotropically disordered sample. This behavior is fundamentally different from the effect of a direct intermolecular dipolar coupling, which shows an opposite rate modification tendency for the para and anti-para dipole orientations. When the vibrational frequencies of two molecules are different, the cavity-mediated intermolecular reaction channel will be blocked. Thus, as expected, we don't observe a collective rate enhancement effect in a heterodimer model.

As a final remark, in experiments, a macroscopic number of molecules can be collectively coupled to a collection of cavity modes. To attain a deeper and more robust understanding of the collective effect, we plan to employ the HEOM method in conjunction with a more advanced tensor network state approach in our future work.<sup>63</sup> This approach will enable us to consider a much larger model involving a dozen molecules inside the cavity.

## ACKNOWLEDGMENTS

The authors appreciate valuable discussions with Marit Fiechter and Joseph Lawrence.

TABLE II. Eigenenergies of the bare molecule for two different masses:  $M = 0.5$  a.u. and  $M = 4$  a.u. .

$\epsilon_k^{\text{mol}}$ (cm <sup>-1</sup> )	$\epsilon_0^{\text{mol}}$	$\epsilon_1^{\text{mol}}$	$\epsilon_2^{\text{mol}}$	$\epsilon_3^{\text{mol}}$	$\epsilon_4^{\text{mol}}$	$\epsilon_5^{\text{mol}}$	$\epsilon_6^{\text{mol}}$	$\epsilon_7^{\text{mol}}$
$M = 0.5$ a.u.	921	948	2266	2738	3727	4773	5964	7260
$M = 4$ a.u.	346	346	1007	1007	1606	1609	2090	2148

## SUPPLEMENTARY INFORMATION

See the supplementary material for the details of (1) Matrix representation of the transition dipole moment for different models; (2) Analysis of the reaction dynamics for Model II inside the cavity with a stronger light-matter interaction  $\eta_c = 0.005$ ; (3) The photon distribution of the cavity mode.

## DATA AVAILABILITY STATEMENT

The data and code that support the findings of this work are available from the corresponding author under reasonable request.

### Appendix A: Single molecule with a mass $M = 0.5$ a.u.

In this appendix, we focus on a single molecule characterized by the same potential energy surface as described in the main text, but with a smaller mass,  $M = 0.5$  a.u. . Consequently, the vibrational frequency increases, resulting in only two eigenstates below the barrier, as illustrated in Fig. 14(a). For the molecule outside the cavity, the reaction proceeds predominantly through the tunneling at the lowest two vibrational states, with a reaction rate on the scale of  $10^{-4}$  fs<sup>-1</sup>. This quickly leads to a dynamical equilibrium of forward and back reaction within tens of picoseconds. The higher vibrationally excited states above the barrier play a relatively minor role in the reaction for this model, and their involvement leads to a slight decrease in the reaction rate, as depicted in Fig. 14(b). In other words, the resonant vibrational transitions don't contribute significantly to the reaction. This explains our observation in Fig. 14(c) that, the rates inside the cavity are suppressed and the rate profiles present no sharp resonance peak over the entire  $\omega_c$  range.

### Appendix B: Single molecule with a mass $M = 4$ a.u.

Here, we consider a single molecule with a mass of  $M = 4$  a.u. . This model yields eight eigenstates below the barrier, as listed in Table II and shown in Fig. 15(a).

First, we examine the reaction outside the cavity. The tunneling rate at the lowest two vibrational levels is remarkably low, on the order of  $10^{-14}$  fs<sup>-1</sup>. The reaction experiences a three-order-of-magnitude acceleration when considering four vibrational levels ( $N_v^{\text{mol}} = 4$ ). However, the rate remains too small to be visible in Fig. 15(b). With  $N_v^{\text{mol}} = 6$ , there is a noticeable increase in the rate, as shown in Fig. 15(b), attributed

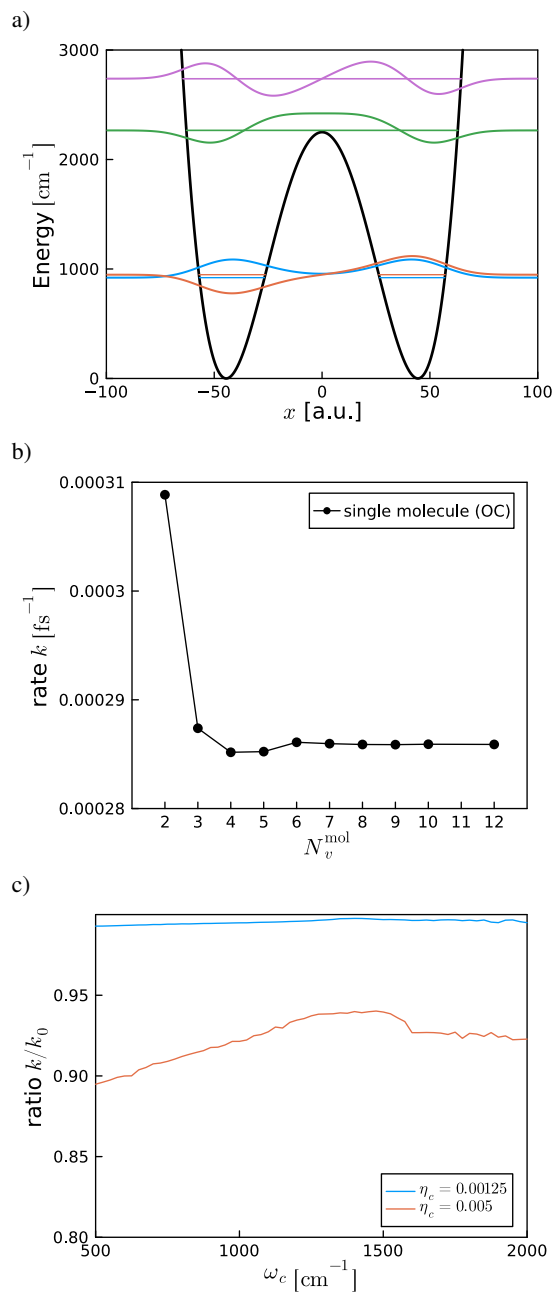


FIG. 14. a) Potential energy surface, eigenenergies, and eigenstates for the bare molecule with a mass of  $M = 0.5$  a.u.. b) Reaction rate  $k$  as a function of the number of  $N_v^{\text{mol}}$  for a single molecule outside the cavity (OC). c) Rate modification profile  $k/k_0$  as a function of the cavity frequency  $\omega_c$  with two different light-matter interaction strengths  $\eta_c$ . Here  $k_0$  denotes the reaction rate of a single molecule outside the cavity. The results are obtained with  $N_v^{\text{cav}} = 10$  and  $N_v^{\text{mol}} = 12$ .

to the vibrational heating and a much faster tunneling rate at the vibrational states  $|v_4^{\text{mol}}\rangle$  and  $|v_5^{\text{mol}}\rangle$ . A significant leap of the rate occurs when  $N_v^{\text{mol}}$  is increased to 8, owing to ultrafast tunneling near the barrier top. At this point, the rate reaches the same order of magnitude of the converged rate constant,  $k = 1.2 \times 10^{-7} \text{ fs}^{-1}$ , which is obtained with  $N_v^{\text{mol}} = 12$ .

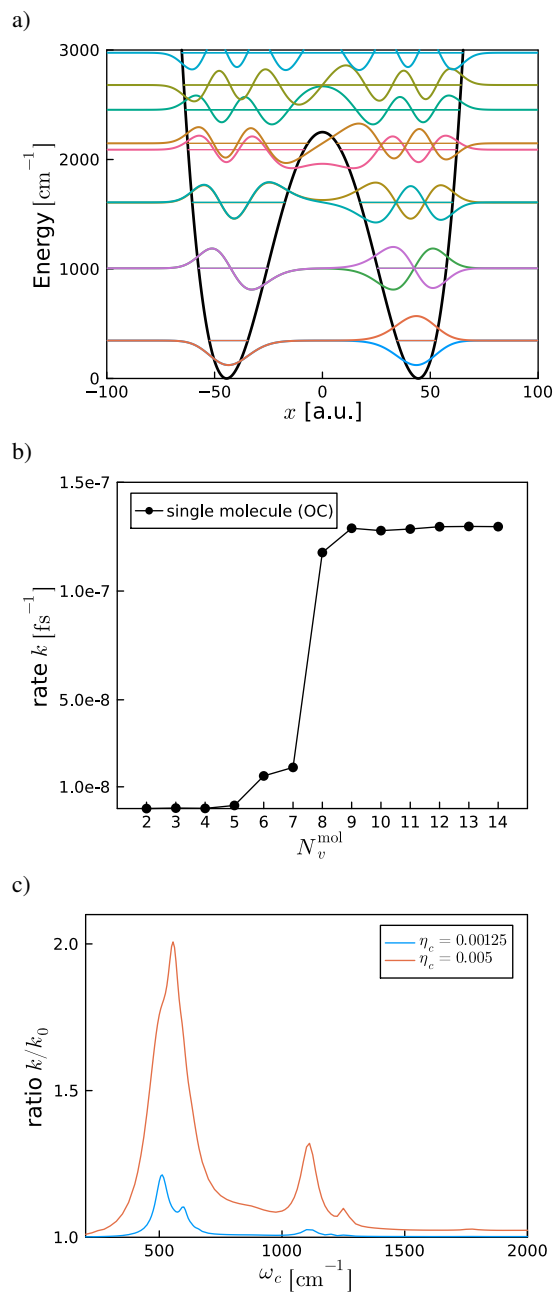


FIG. 15. Same as Fig. 14 except that the mass is  $M = 4$  a.u..

Placing this molecule inside the cavity and considering two light-matter coupling strengths,  $\eta_c = 0.00125$  and  $\eta_c = 0.005$ , we calculate the reaction rate  $k$  over a broader cavity range from  $\omega_c = 200 \text{ cm}^{-1}$  to  $\omega_c = 2000 \text{ cm}^{-1}$ . The results are displayed in Fig. 15(b). Three prominent peaks are observed at around  $510 \text{ cm}^{-1}$ ,  $600 \text{ cm}^{-1}$ , and  $1115 \text{ cm}^{-1}$  for  $\eta_c = 0.00125$ . Based on the analysis of the energy gaps between different vibrational levels in combination with the transition matrix  $\langle v_{k'}^{\text{mol}} | x | v_k^{\text{mol}} \rangle$  (provided in the SI), we can assign the peak at  $510 \text{ cm}^{-1}$  to the photon-assisted vibrational transitions between  $v_4^{\text{mol}} \leftrightarrow v_7^{\text{mol}}$  and  $v_5^{\text{mol}} \leftrightarrow v_6^{\text{mol}}$ . The peak at  $600 \text{ cm}^{-1}$  is associated with the vibrational transitions  $v_2^{\text{mol}} \leftrightarrow v_5^{\text{mol}}$  and

$\nu_3^{\text{mol}} \leftrightarrow \nu_4^{\text{mol}}$ . The other peak in the high-frequency end around  $\omega_c = 1115 \text{ cm}^{-1}$  is attributed to the photon-assisted vibrational transitions  $\nu_2^{\text{mol}} \leftrightarrow \nu_7^{\text{mol}}$  and  $\nu_3^{\text{mol}} \leftrightarrow \nu_6^{\text{mol}}$ . There is also a small peak at  $1255 \text{ cm}^{-1}$ , which is not readily visible with  $\eta_c = 0.00125$ , but becomes more apparent when the light-matter coupling strength is increased to,  $\eta_c = 0.005$ . It is related to the vibrational transitions,  $\nu_0^{\text{mol}} \leftrightarrow \nu_5^{\text{mol}}$  and  $\nu_1^{\text{mol}} \leftrightarrow \nu_4^{\text{mol}}$ . Besides, two peaks in the lower frequency regime merge and form a strong peak in the middle at  $555 \text{ cm}^{-1}$  for the stronger  $\eta_c = 0.005$ , due to the additional broadening effect brought in by the cavity mode and the cavity bath. It is worth noting that a photon with the frequency  $\omega_c = 660 \text{ cm}^{-1}$  induces the vibrational transitions  $\nu_0^{\text{mol}} \leftrightarrow \nu_3^{\text{mol}}$  and  $\nu_1^{\text{mol}} \leftrightarrow \nu_2^{\text{mol}}$ , opening up a cotunneling path. However, we don't observe a conspicuous peak in Fig. 15(c) at the supposed frequency. This is because the tunneling rate from the left well to the right well on the states  $|v_2^{\text{mol}}\rangle$  and  $|v_3^{\text{mol}}\rangle$  is much slower than the reaction rate outside the cavity  $k_0$ . As such, the rate enhancement effect is nearly negligible.

- <sup>1</sup>A. Thomas, J. George, A. Shalabney, M. Dryzhakov, S. J. Varma, J. Moran, T. Chervy, X. Zhong, E. Devaux, C. Genet, *et al.*, "Ground-state chemical reactivity under vibrational coupling to the vacuum electromagnetic field," *Angew. Chem.-ger. Edit.* **128**, 11634–11638 (2016).
- <sup>2</sup>R. M. Vergauwe, A. Thomas, K. Nagarajan, A. Shalabney, J. George, T. Chervy, M. Seidel, E. Devaux, V. Torbeev, and T. W. Ebbesen, "Modification of enzyme activity by vibrational strong coupling of water," *Angew. Chem. - Int. Ed.* **58**, 15324–15328 (2019).
- <sup>3</sup>J. Lather, P. Bhatt, A. Thomas, T. W. Ebbesen, and J. George, "Cavity catalysis by cooperative vibrational strong coupling of reactant and solvent molecules," *Angew. Chem. - Int. Ed.* **58**, 10635–10638 (2019).
- <sup>4</sup>A. Thomas, L. Lethuillier-Karl, K. Nagarajan, R. M. Vergauwe, J. George, T. Chervy, A. Shalabney, E. Devaux, C. Genet, J. Moran, *et al.*, "Tilting a ground-state reactivity landscape by vibrational strong coupling," *Science* **363**, 615–619 (2019).
- <sup>5</sup>H. Hiura, A. Shalabney, and J. George, "Vacuum-field catalysis: Accelerated reactions by vibrational ultra strong coupling," (2019).
- <sup>6</sup>A. Thomas, A. Jayachandran, L. Lethuillier-Karl, R. M. Vergauwe, K. Nagarajan, E. Devaux, C. Genet, J. Moran, and T. W. Ebbesen, "Ground state chemistry under vibrational strong coupling: dependence of thermodynamic parameters on the rabi splitting energy," *Proc. Spie.* **9**, 249–255 (2020).
- <sup>7</sup>K. Hirai, J. A. Hutchison, and H. Uji-i, "Recent progress in vibropolaritonic chemistry," *ChemPlusChem* **85**, 1981–1988 (2020).
- <sup>8</sup>K. Hirai, R. Takeda, J. A. Hutchison, and H. Uji-i, "Modulation of prins cyclization by vibrational strong coupling," *Angew. Chem.-ger. Edit.* **132**, 5370–5373 (2020).
- <sup>9</sup>A. Sau, K. Nagarajan, B. Patraha, L. Lethuillier-Karl, R. M. Vergauwe, A. Thomas, J. Moran, C. Genet, and T. W. Ebbesen, "Modifying woodward–hoffmann stereoselectivity under vibrational strong coupling," *Angew. Chem. - Int. Ed.* **60**, 5712–5717 (2021).
- <sup>10</sup>J. Lather, A. N. Thabassum, J. Singh, and J. George, "Cavity catalysis: modifying linear free-energy relationship under cooperative vibrational strong coupling," *Chem. Sci.* **13**, 195–202 (2022).
- <sup>11</sup>W. Ahn, J. F. Triana, F. Recabal, F. Herrera, and B. S. Simpkins, "Modification of ground-state chemical reactivity via light–matter coherence in infrared cavities," *Science* **380**, 1165–1168 (2023).
- <sup>12</sup>T. W. Ebbesen, "Hybrid light–matter states in a molecular and material science perspective," *Accounts Chem. Res.* **49**, 2403–2412 (2016).
- <sup>13</sup>R. F. Ribeiro, L. A. Martínez-Martínez, M. Du, J. Campos-Gonzalez-Angulo, and J. Yuen-Zhou, "Polariton chemistry: controlling molecular dynamics with optical cavities," *Chem. Sci.* **9**, 6325–6339 (2018).
- <sup>14</sup>K. Nagarajan, A. Thomas, and T. W. Ebbesen, "Chemistry under vibrational strong coupling," *J. Am. Chem. Soc.* **143**, 16877–16889 (2021).
- <sup>15</sup>J. Galego, F. J. Garcia-Vidal, and J. Feist, "Suppressing photochemical reactions with quantized light fields," *Nat. Commun.* **7**, 13841 (2016).
- <sup>16</sup>J. Galego, F. J. Garcia-Vidal, and J. Feist, "Many-molecule reaction triggered by a single photon in polaritonic chemistry," *Phys. Rev. Lett.* **119**, 136001 (2017).
- <sup>17</sup>J. Galego, C. Climent, F. J. Garcia-Vidal, and J. Feist, "Cavity casimir-polder forces and their effects in ground-state chemical reactivity," *Phys. Rev. X* **9**, 021057 (2019).
- <sup>18</sup>J. A. Campos-Gonzalez-Angulo and J. Yuen-Zhou, "Polaritonic normal modes in transition state theory," *J. Chem. Phys.* **152** (2020).
- <sup>19</sup>A. Mandal, S. Montillo Vega, and P. Huo, "Polarized fock states and the dynamical casimir effect in molecular cavity quantum electrodynamics," *J. Phys. Chem. Lett.* **11**, 9215–9223 (2020).
- <sup>20</sup>P.-Y. Yang and J. Cao, "Quantum effects in chemical reactions under polaritonic vibrational strong coupling," *J. Phys. Chem. Lett.* **12**, 9531–9538 (2021).
- <sup>21</sup>X. Li, A. Mandal, and P. Huo, "Theory of mode-selective chemistry through polaritonic vibrational strong coupling," *J. Phys. Chem. Lett.* **12**, 6974–6982 (2021).
- <sup>22</sup>T. E. Li, A. Nitzan, and J. E. Subotnik, "On the origin of ground-state vacuum-field catalysis: Equilibrium consideration," *J. Chem. Phys.* **152**, 234107 (2020).
- <sup>23</sup>X. Li, A. Mandal, and P. Huo, "Cavity frequency-dependent theory for vibrational polariton chemistry," *Nat. Commun.* **12**, 1315 (2021).
- <sup>24</sup>J. Sun and O. Vendrell, "Suppression and enhancement of thermal chemical rates in a cavity," *J. Phys. Chem. Lett.* **13**, 4441–4446 (2022).
- <sup>25</sup>C. Schäfer, J. Flick, E. Ronca, P. Narang, and A. Rubio, "Shining light on the microscopic resonant mechanism responsible for cavity-mediated chemical reactivity," *Nat. Commun.* **13**, 7817 (2022).
- <sup>26</sup>A. Mandal, X. Li, and P. Huo, "Theory of vibrational polariton chemistry in the collective coupling regime," *J. Chem. Phys.* **156** (2022).
- <sup>27</sup>L. P. Lindoy, A. Mandal, and D. R. Reichman, "Resonant cavity modification of ground-state chemical kinetics," *J. Phys. Chem. Lett.* **13**, 6580–6586 (2022).
- <sup>28</sup>D. S. Wang, T. Neuman, S. F. Yelin, and J. Flick, "Cavity-modified unimolecular dissociation reactions via intramolecular vibrational energy redistribution," *J. Phys. Chem. Lett.* **13**, 3317–3324 (2022).
- <sup>29</sup>E. W. Fischer, J. Anders, and P. Saalfrank, "Cavity-altered thermal isomerization rates and dynamical resonant localization in vibro-polaritonic chemistry," *J. Chem. Phys.* **156**, 154305 (2022).
- <sup>30</sup>M. R. Fiechter, J. E. Runeson, J. E. Lawrence, and J. O. Richardson, "How quantum is the resonance behavior in vibrational polariton chemistry?" *J. Phys. Chem. Lett.* **14**, 8261–8267 (2023).
- <sup>31</sup>I. Sokolovskii and G. Groenhof, "Non-hermitian molecular dynamics simulations of exciton-polaritons in lossy cavities," arXiv preprint arXiv:2311.13453 (2023).
- <sup>32</sup>F. Pavošević, R. L. Smith, and A. Rubio, "Computational study on the catalytic control of endo/exo diels-alder reactions by cavity quantum vacuum fluctuations," *Nat. Commun.* **14**, 2766 (2023).
- <sup>33</sup>D. Hu, W. Ying, and P. Huo, "Resonance enhancement of vibrational polariton chemistry obtained from the mixed quantum-classical dynamics simulations," *J. Phys. Chem. Lett.* **14**, 11208–11216 (2023).
- <sup>34</sup>A. Mandal, M. A. Taylor, B. M. Weight, E. R. Koessler, X. Li, and P. Huo, "Theoretical advances in polariton chemistry and molecular cavity quantum electrodynamics," *Chem. Rev.* **123**, 9786–9879 (2023).
- <sup>35</sup>J. Fregoni, F. J. Garcia-Vidal, and J. Feist, "Theoretical challenges in polaritonic chemistry," *ACS Photonics* **9**, 1096–1107 (2022).
- <sup>36</sup>J. Campos-Gonzalez-Angulo, Y. Poh, M. Du, and J. Yuen-Zhou, "Swinging between shine and shadow: Theoretical advances on thermally activated vibropolaritonic chemistry," *J. Chem. Phys.* **158**, 230901–230901 (2023).
- <sup>37</sup>L. P. Lindoy, A. Mandal, and D. R. Reichman, "Quantum dynamical effects of vibrational strong coupling in chemical reactivity," *Nat. Commun.* **14**, 2733 (2023).
- <sup>38</sup>W. Ying and P. Huo, "Resonance theory and quantum dynamics simulations of vibrational polariton chemistry," *J. Chem. Phys.* **159**, 084104 (2023).
- <sup>39</sup>R. Borrelli, "Density matrix dynamics in twin-formulation: An efficient methodology based on tensor-train representation of reduced equations of motion," *J. Chem. Phys.* **150**, 234102 (2019).
- <sup>40</sup>R. Borrelli and M. F. Gelin, "Finite temperature quantum dynamics of complex systems: Integrating thermo-field theories and tensor-train methods," *WIREs Comput Mol Sci* , e1539 (2021).
- <sup>41</sup>Y. Ke, R. Borrelli, and M. Thoss, "Hierarchical equations of motion ap-

- proach to hybrid fermionic and bosonic environments: Matrix product state formulation in twin space,” *J. Chem. Phys.* **156**, 194102 (2022).
- <sup>42</sup>U. Schollwöck, “The density-matrix renormalization group in the age of matrix product states,” *Ann. Phys. (NY)* **326**, 96–192 (2011).
- <sup>43</sup>I. V. Oseledets, “Tensor-train decomposition,” *SIAM J. Sci. Comput.* **33**, 2295–2317 (2011).
- <sup>44</sup>J. Haegeman, C. Lubich, I. Oseledets, B. Vandereycken, and F. Verstraete, “Unifying time evolution and optimization with matrix product states,” *Phys. Rev. B* **94**, 165116 (2016).
- <sup>45</sup>S. Paecel, T. Köhler, A. Swoboda, S. R. Manmana, U. Schollwöck, and C. Hubig, “Time-evolution methods for matrix-product states,” *Ann. Phys. (NY)* **411**, 167998 (2019).
- <sup>46</sup>A. J. Dunnett and A. W. Chin, “Efficient bond-adaptive approach for finite-temperature open quantum dynamics using the one-site time-dependent variational principle for matrix product states,” *Phys. Rev. B* **104**, 214302 (2021).
- <sup>47</sup>J. Flick, M. Ruggenthaler, H. Appel, and A. Rubio, “Atoms and molecules in cavities, from weak to strong coupling in quantum-electrodynamics (QED) chemistry,” *Proc. Natl. Acad. Sci. USA* **114**, 3026–3034 (2017).
- <sup>48</sup>V. Rokaj, D. M. Welakuh, M. Ruggenthaler, and A. Rubio, “Light–matter interaction in the long-wavelength limit: no ground-state without dipole self-energy,” *J. Phys. B: At. Mol. Opt. Phys.* **51**, 034005 (2018).
- <sup>49</sup>Y. Tanimura and R. Kubo, “Time evolution of a quantum system in contact with a nearly gaussian-markoffian noise bath,” *J. Phys. Soc. Jpn.* **58**, 101–114 (1989).
- <sup>50</sup>Y.-a. Yan, F. Yang, Y. Liu, and J. Shao, “Hierarchical approach based on stochastic decoupling to dissipative systems,” *Chem. Phys. Lett.* **395**, 216–221 (2004).
- <sup>51</sup>R.-X. Xu and Y. Yan, “Dynamics of quantum dissipation systems interacting with bosonic canonical bath: Hierarchical equations of motion approach,” *Phys. Rev. E* **75**, 031107 (2007).
- <sup>52</sup>Q. Shi, L. Chen, G. Nan, R.-X. Xu, and Y. Yan, “Efficient hierarchical liouville space propagator to quantum dissipative dynamics,” *J. Chem. Phys.* **130**, 084105 (2009).
- <sup>53</sup>Y. Tanimura, “Numerically “exact” approach to open quantum dynamics: The hierarchical equations of motion (HEOM),” *J. Chem. Phys.* **153**, 020901 (2020).
- <sup>54</sup>J. Hu, R.-X. Xu, and Y. Yan, “Communication: Padé spectrum decomposition of Fermi function and Bose function,” *J. Chem. Phys.* **133**, 101106 (2010).
- <sup>55</sup>M. Xu, Y. Yan, Q. Shi, J. Ankerhold, and J. Stockburger, “Taming quantum noise for efficient low temperature simulations of open quantum systems,” *Phys. Rev. Lett.* **129**, 230601 (2022).
- <sup>56</sup>W. H. Miller, S. D. Schwartz, and J. W. Tromp, “Quantum mechanical rate constants for bimolecular reactions,” *J. Chem. Phys.* **79**, 4889–4898 (1983).
- <sup>57</sup>I. R. Craig, M. Thoss, and H. Wang, “Proton transfer reactions in model condensed-phase environments: Accurate quantum dynamics using the multilayer multiconfiguration time-dependent Hartree approach,” *J. Chem. Phys.* **127**, 144503 (2007).
- <sup>58</sup>L. Chen and Q. Shi, “Quantum rate dynamics for proton transfer reactions in condensed phase: The exact hierarchical equations of motion approach,” *J. Chem. Phys.* **130**, 134505 (2009).
- <sup>59</sup>Y. Ke, C. Kaspar, A. Erpenbeck, U. Peskin, and M. Thoss, “Nonequilibrium reaction rate theory: Formulation and implementation within the hierarchical equations of motion approach,” *J. Chem. Phys.* **157**, 034103 (2022).
- <sup>60</sup>D. T. Colbert and W. H. Miller, “A novel discrete variable representation for quantum mechanical reactive scattering via the S-matrix kohn method,” *J. Chem. Phys.* **96**, 1982–1991 (1992).
- <sup>61</sup>J. Echave and D. C. Clary, “Potential optimized discrete variable representation,” *Chem. Phys. Lett.* **190**, 225–230 (1992).
- <sup>62</sup>C. Schafer, M. Ruggenthaler, V. Rokaj, and A. Rubio, “Relevance of the quadratic diamagnetic and self-polarization terms in cavity quantum electrodynamics,” *ACS Photonics* **7**, 975–990 (2020).
- <sup>63</sup>Y. Ke, “Tree tensor network state approach for solving hierarchical equations of motion,” *J. Chem. Phys.* **158**, 211102 (2023).